

Slave-boson Formalism for Superconducting Pairing at Strong Coupling

Sarbjit Mazumdar,¹ Jonas Issing,¹ Jannis Seufert,¹ David Riegler,^{2,1} Peter Wölfle,² Ronny Thomale,¹ and Michael Klett^{1,*}

¹*Institut für Theoretische Physik und Astrophysik and Würzburg-Dresden Cluster of Excellence ctd.qmat, Julius-Maximilians-Universität Würzburg, Am Hubland, Campus Süd, Würzburg 97074, Germany*

²*Institut für Theorie der Kondensierten Materie, Karlsruhe Institute of Technology, D-76128 Karlsruhe, Germany*

(Dated: May 27, 2026)

We study the emergence of superconductivity in the one-band Hubbard model using the spin-rotation-invariant Kotliar–Ruckenstein slave-boson (SB) approach. Motivated by its intrinsically renormalized mean-field ground state, we construct an effective pairing vertex from dynamical fluctuations about the saddle point. Solving the anisotropic, frequency-dependent gap equation on the square lattice, we map the pairing instabilities across doping, interaction, temperature and real-frequency gap structure that qualitatively match experimental cuprate observations. This framework merges strong-correlation SB-type renormalizations with RPA-type pairing transparency, providing a scalable route to modeling multi-orbital superconductivity at strong coupling.

I. INTRODUCTION

Strongly correlated electron systems host a broad range of emergent phases, including charge and spin ordered states, unconventional superconductivity, and correlated metals with properties beyond conventional order. Strategies for solving this analytically non-tractable problem center around (i) model simplification and (ii) designing numerical ways to address the strong electronic interactions. A central minimal setting is the single-band Hubbard model on the square lattice with nearest- and next-nearest-neighbor hopping, widely used as a controlled arena for cuprate-inspired physics. Across complementary numerical approaches, robust evidence has accumulated for dominant d -wave pairing tendencies near intermediate fillings, including quantum Monte Carlo (QMC)[1–3], density-matrix renormalization group (DMRG) studies on ladders and wide cylinders [4–6], density-matrix embedding theory (DMET) [7, 8], and renormalization-group (RG) benchmarks [9–12]. At the same time, a unified description that connects pairing symmetry, fluctuation spectra, and dynamical gap structure across the broad interaction and doping ranges of interest remains an open challenge.

A key conceptual milestone is the observation that superconductivity can arise even from purely repulsive interactions by Kohn and Luttinger [13, 14]. In lattice settings, the prevalent physical picture is that pairing is promoted by the exchange of collective fluctuations, most prominently spin fluctuations. Within this framework, Berk and Schrieffer, along with later works by Scalapino et al., established the connection between enhanced magnetic response and unconventional pairing [15–17]. Random-phase-approximation (RPA)-based treatments make this mechanism particularly transparent yet constrain their ability to reproduce many quali-

tative features of the ensuing phase diagrams to weak-to-intermediate-coupling [18–21]. In particular for intermediate and strong coupling, the predictive power of such approaches hinges on the accuracy of the underlying dynamical susceptibilities, as capturing both their strong-correlation renormalizations and their full frequency dependence is essential for controlled statements about pairing kernels and the resulting frequency-dependent order parameter.

Gauged by field activity, dynamical mean field theory [22–25] (DMFT) lends itself as a preferred modern-day numerical approach to address such a problem out-set of correlated electron systems, where strong dynamical fluctuations are crucial and safely assumed to be mainly local. As unconventional pairing specifically entails non-local correlators emanating from non-local fluctuations, however, it is desirable to achieve a methodological ansatz which generically incorporates dynamical non-local fluctuations and is numerically efficient to allow large scale scans to access multi-parametric phase diagrams. While significant progress has been made within DMFT to include non-local correlations [26], it does remain rather involved in terms of technicality and numerical effort, and hence keeps challenging the quantitative access to non-local phenomena of strongly correlated electron systems such as unconventional superconductivity.

The Gutzwiller wave function [27–29] offers a compact variational route to incorporate correlations while retaining itinerancy. Its key insight is that by suppressing costly double occupancies via a local projector, it reduces the probabilistic weight of hopping processes that would create them, thereby inherently capturing bandwidth renormalization and Mott physics [30, 31]. The Kotliar–Ruckenstein slave-boson (KR-SB) formulation translates this variational insight into an explicit fermionic operator framework by introducing auxiliary bosons that resolve the local occupancy configurations (empty, singly, doubly occupied), recovering the Gutzwiller approximation at the mean-field saddle point

* michael.klett@uni-wuerzburg.de

[32]. Its spin-rotation-invariant generalization (SRIKR) [33, 34] enables a consistent treatment of commensurate and incommensurate collective spin and charge dynamics as well as renormalizing the underlying band structure [35, 36]. Importantly, Gaussian fluctuations around this correlated saddle point yield fully dynamical susceptibilities that already encode strong-correlation renormalizations at both quasiparticle and vertex levels—originating from a correlated reference state rather than bare-band propagators. This marks a conceptual departure from RPA-type treatments, providing a starting point that already incorporates medium to strong-correlation at the quasiparticle and vertex level for the subsequent pairing analysis.

In this Article, we leverage dynamical slave-boson susceptibilities to construct an effective two-particle pairing vertex that is explicitly antisymmetric under fermionic exchange and decomposes into density/spin and singlet/triplet channels. Using this vertex, we solve the anisotropic, frequency-dependent gap equation on the square lattice and classify leading pairing symmetries across doping, interaction strength, and temperature, revealing spin-fluctuation dominance and d -wave phase evolution in quantitative agreement with available numerical benchmarks and experimental observations in cuprates. We find that the pairing kernel is generically dominated by the spin-fluctuation channel, yielding a systematic superconducting symmetry map, and extract real-frequency gap features via Padé continuation of Matsubara-axis solutions. The framework we unfold here provides a direct, scalable route from slave-boson fluctuation dynamics to superconducting pairing, suggests immediate applicability to strong coupling, and renders itself naturally extensible to multi-orbital settings.

The article is organized as follows. In Section II we introduce the principal methodological and model starting point, as we particularize to the single band Hubbard model on the square lattice and expand on the elementary properties of the effective two-particle vertex and the superconducting gap equation from the viewpoint of slave boson mean field theory. For the sake of readability most technical details are delegated to the appendices contained in the extensive supplementary material. Section III continues by elaborating on the results we have achieved, starting with the spin/charge fluctuation profile, the phase diagram as a function of filling n and Hubbard U . This is then followed up by moving to superconductivity, where we resolve the filling dependence of superconductivity seeded by strong coupling fluctuations, the critical temperature, and the dynamical gap profile. We conclude in Section IV that our framework establishes a promising new angle at strong coupling superconductivity, and outline several research threads for future work.

II. MODEL & METHOD

We study the single-band Hubbard model on the two-dimensional square lattice, which captures the fundamental competition between electron itinerancy and strong local correlations through nearest-neighbor hopping and on-site Coulomb repulsion [27, 37, 38]. This model serves as a paradigmatic framework for understanding emergent phenomena in correlated electron systems, providing a minimal yet nontrivial setting in which magnetism, Mott insulating behavior, and unconventional superconductivity naturally arise. In the context of cuprate superconductors, effective one-band descriptions of the CuO_2 planes have established the Hubbard model as a widely used minimal starting point [39, 40]. Around half filling, the model exhibits antiferromagnetic order, and upon doping, it develops strong magnetic fluctuations that can promote d -wave pairing. Its properties have been extensively benchmarked across complementary numerical methods, ensuring a reliable reference for further methodological development and comparison. The corresponding Hamiltonian is given by,

$$\begin{aligned} \mathcal{H} &= - \sum_{ij\sigma} t_{ij} c_{i\sigma}^\dagger c_{j\sigma} + U \sum_i n_{i\uparrow} n_{i\downarrow} - \mu \sum_{i\sigma} n_{i\sigma} \\ &= \sum_{\mathbf{k}\sigma} (\epsilon_{\mathbf{k}} - \mu) c_{\mathbf{k}\sigma}^\dagger c_{\mathbf{k}\sigma} + U \sum_i n_{i\uparrow} n_{i\downarrow}. \end{aligned} \quad (1)$$

where $c_{i\sigma}^\dagger$ ($c_{i\sigma}$) creates (annihilates) an electron with spin σ on lattice site i . Analogously, $c_{\mathbf{k}\sigma}^{(\dagger)}$ denotes the Fourier transform of $c_{i\sigma}^{(\dagger)}$ and acts in momentum space. Here, $\epsilon_{\mathbf{k}}$ is the single-particle dispersion defining the band structure, μ is the chemical potential controlling the electron filling, and $n_{i\sigma} = c_{i\sigma}^\dagger c_{i\sigma}$ is the number operator for electrons with spin σ at site i . The nearest-neighbor hopping sets the energy unit, t , and we also include a next-nearest-neighbor hopping t' . All energy scales are given in units of t . The Gutzwiller projection, a well-established variational mean-field approach capturing Mott physics and bandwidth renormalization, serves as our starting point [30, 31]. We build upon it via the spin-rotation-invariant Kotliar–Ruckenstein (SRIKR) slave-boson representation, enabling Gaussian fluctuations around the paramagnetic saddle to yield physically motivated dynamical susceptibilities for the pairing vertex. The physical electron is

$$c_{i\sigma}^\dagger = \sum_{\sigma'} z_{i,\sigma\sigma'}^\dagger f_{i,\sigma'}^\dagger, \quad (2)$$

with pseudofermions $f_{i\sigma}^{(\dagger)}$ and bosons $e_i, d_i, p_{i\alpha}$ ($\alpha = 0, 1, 2, 3$) projecting local occupancies (empty, double, single). The renormalization matrix $z(e, p, d)$ encodes Gutzwiller factors, preserves $\text{SU}(2)$ spin rotation symmetry, and recovers the noninteracting limit. Local constraints restrict to the physical Hilbert space; we refer to the corresponding Lagrange multipliers and bosons

representing occupancies as bosonic fields ψ . To obtain response functions, we consider Gaussian fluctuations about the paramagnetic saddle point [41, 42] and expand the action (\mathcal{S}) to quadratic order in the bosonic fields ψ_μ :

$$\delta\mathcal{S}^{(2)} = \sum_{\mathbf{q},n} \delta\psi_\mu(-q) \mathcal{M}_{\mu\nu}(q) \delta\psi_\nu(q), \quad (3)$$

with fluctuation matrix

$$\mathcal{M}_{\mu\nu}(q) := \frac{\delta^2\mathcal{S}(\psi)}{\delta\psi_\mu(-q)\delta\psi_\nu(q)}, \quad (4)$$

where $q = (\mathbf{q}, i\Omega_n)$ and $\Omega_n = 2\pi nT$ ($n \in \mathbb{Z}$) is a bosonic Matsubara frequency. From this we can compute charge and spin susceptibilities. The spin (s) and charge (c) susceptibilities arising from the fluctuation expansion are linear combinations of different elements of the inverse fluctuation matrix \mathcal{M}

$$\chi_{s/c}(q) = \sum_{\mu,\nu} \mathcal{E}_{s/c}^{\mu,\nu} \mathcal{M}_{\mu\nu}^{-1}(q). \quad (5)$$

where $\mathcal{E}_{s/c}^{\mu,\nu}$ are susceptibility-dependent form factors. The static spin and charge susceptibilities are obtained at the lowest bosonic Matsubara frequency, $i\Omega_0 = 0$:

$$\chi_{s/c}(\mathbf{q}) = \chi_{s/c}(\mathbf{q}, i\Omega_0). \quad (6)$$

We further introduce the bare susceptibility $\chi_0(q)$ as the Lindhard bubble of renormalized pseudofermion bands. Details can be found in the Supplemental Materials Sec. S1 as well as in references [43, 44].

A. Pair interaction

To access the Cooper channel generated by a purely repulsive local interaction, we integrate out particle-hole fluctuations and work with the resulting two-particle irreducible pairing kernel. In the spirit of the Kohn-Luttinger construction [13, 14], the leading nontrivial contribution arises at second order in interaction from the exchange of collective spin and charge modes. In the present approach these modes are encoded by the SB susceptibilities χ_s and χ_c , which therefore provide the natural building blocks for the fluctuation-mediated effective pairing vertex (following a RPA-like resummation [15–17]) used below. In order to construct the effective pair interaction derived from the exchange of spin or charge fluctuations, we need to know the vertex functions $\mathcal{K}_{s,c}(q)$ coupling the quasiparticles to the fluctuations. In diagrammatic language, these are given by the particle-hole irreducible vertex functions in the respective channels [45]. Within the slave-boson framework, we identify their effective counterparts by rewriting the susceptibilities in an RPA-like form,

$$\chi_{s,c}(q) = \frac{\chi_0(q)}{1 - \mathcal{K}_{s,c}(q)\chi_0(q)}, \quad (7)$$

where $\chi_0(q)$ is the Lindhard susceptibility of the renormalized slave-boson mean-field quasiparticles. Inverting Eq. (7) gives

$$\mathcal{K}_{s,c}(q) = \frac{\chi_{s,c}(q) - \chi_0(q)}{\chi_{s,c}(q)\chi_0(q)}. \quad (8)$$

This procedure extracts the effective quasiparticle-fluctuation vertices $\mathcal{K}_{s,c}$ from the slave-boson response functions. The Cooper-channel pairing interaction is then constructed from the exchange of the corresponding collective propagators. With the normalization used here, the singlet and triplet pairing $\mathcal{V}_{s/t}(q)$ kernels can then be written as

$$\mathcal{V}_s(q) = \mathcal{K}_{\text{irr}}(q) + \frac{3}{2}\mathcal{K}_s^2(q)\chi_s(q) - \frac{1}{2}\mathcal{K}_c^2(q)\chi_c(q). \quad (9)$$

$$\mathcal{V}_t(q) = -\frac{1}{2}\mathcal{K}_s^2(q)\chi_s(q) - \frac{1}{2}\mathcal{K}_c^2(q)\chi_c(q), \quad (10)$$

See Supplemental Material Sec. S2 for more details. Here $\mathcal{K}_{\text{irr}}(q)$ denotes the residual fully irreducible contribution to the singlet Cooper-channel interaction, i.e., the part not generated by exchange of spin or charge fluctuations. In the bare Hubbard RPA limit this term reduces to the first-order onsite repulsion, $\mathcal{K}_{\text{irr}} = U$. In the present slave-boson formulation it is renormalized by the correlated quasiparticle background. Since our focus is on unconventional sign-changing pairing channels, this local residual contribution does not drive nor hinder such instabilities. We can therefore just absorb its scale into the effective onsite interaction when analyzing the fluctuation-mediated part of the pairing kernel. In the later evaluations we will focus on the exchange of spin fluctuations as the principal mechanism of superconductivity. We assess an effective onsite scale by evaluating the spin vertex at the dominant magnetic wave vector, $U_{\text{eff}} = \mathcal{K}_s(\mathbf{Q}, 0)$, where \mathbf{Q} denotes the wave vector (including symmetry-related equivalents) at which the static spin response $\chi_s(\mathbf{q}, 0)$ is maximal. Equivalently,

$$U_{\text{eff}} = \frac{\chi_s(\mathbf{Q}, 0) - \chi_0(\mathbf{Q}, 0)}{\chi_s(\mathbf{Q}, 0)\chi_0(\mathbf{Q}, 0)}. \quad (11)$$

This definition ties the pairing scale to the strongest magnetic fluctuation channel of the slave-boson paramagnetic reference state. The explicit singlet/triplet projection of the antisymmetrized two-particle vertex contains both transferred four-momenta $k - k'$ and $k + k'$ (see Supplemental Material Sec. S2). In the present one-band, inversion-symmetric case with zero center-of-mass Cooper pairing and gap functions of definite singlet/triplet parity, the $k + k'$ contribution maps onto the $k - k'$ contribution inside the full Brillouin-zone gap equation [17].

B. Static & Dynamic Gap equations

At finite temperature, the superconducting gap can be obtained from a frequency-dependent (Eliashberg-type)

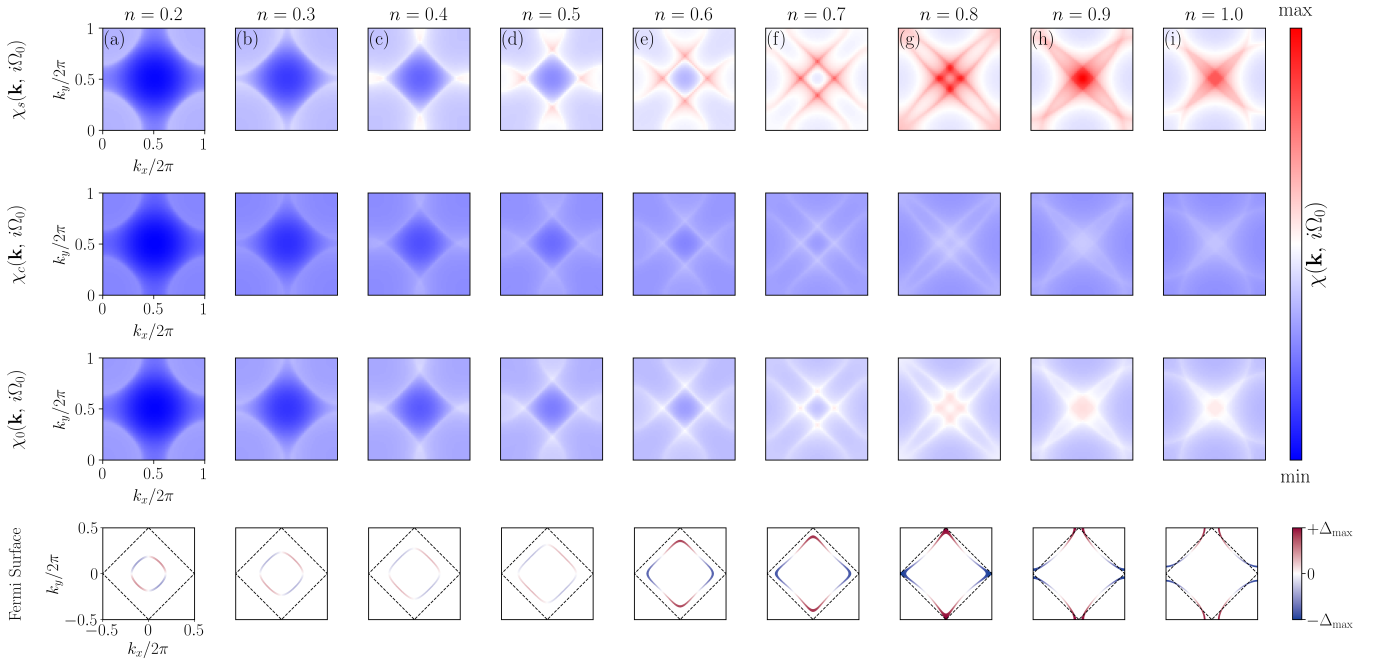


FIG. 1. From top to bottom: static spin, charge, and bare susceptibilities, $\chi_\alpha(\mathbf{k}, i\Omega_0)$ with $\alpha = s, c, 0$, and the leading singlet superconducting instability projected onto the Fermi surface. The panels correspond to fillings $n = 0.2$ to 1.0 [(a)–(i)]. The susceptibility plots are shown on the same color scale to allow direct comparison. In all cases, the spin response exceeds the charge response, indicating spin-fluctuation-dominated pairing. The antiferromagnetic (AF) zone boundary is marked by a black dashed line.

gap equation [20, 21, 46]. For an effective interaction in the singlet/triplet channel, $\mathcal{V}_{s/t}(\mathbf{p}, i\Omega_{nm})$ with bosonic Matsubara frequency $\Omega_{nm} = \omega_n - \omega_m$, the gap function $\Delta_{s/t}(\mathbf{k}, i\omega_n)$ satisfies

$$\Delta_{s/t}(\mathbf{k}, i\omega_n) = -T \sum_{\omega_m} \int \frac{d^2p}{(2\pi)^2} \mathcal{V}_{s/t}(\mathbf{p}, i\Omega_{nm}) \times \frac{\Delta_{s/t}(\mathbf{k} - \mathbf{p}, i\omega_m)}{\omega_m^2 + \xi_{\mathbf{k}-\mathbf{p}}^2 + |\Delta_{s/t}(\mathbf{k} - \mathbf{p}, i\omega_m)|^2}, \quad (12)$$

where $\omega_m = (2m + 1)\pi T$ and $\xi_{\mathbf{k}-\mathbf{p}} = \epsilon_{\mathbf{k}-\mathbf{p}} - \mu$. The momentum-transfer structure of the interaction is crucial because it can promote unconventional, *i.e.* sign-changing anisotropic pairing. In particular, strong antiferromagnetic fluctuations yield a spin susceptibility $\chi_s(\mathbf{q})$ at low frequencies that is peaked near $\mathbf{q} = (\mathbf{Q}, 0)$, thereby enhancing pair scattering with momentum transfer \mathbf{Q} . If \mathbf{Q} connects Fermi-surface regions across which a d -wave form factor changes sign, this mechanism naturally favors d -wave superconductivity. By contrast, although the charge-fluctuation contribution $U_{\text{eff}}^2 \chi_c(q)$ enters with the sign required for attraction, its magnitude in our parameter regime is too small to stabilize a BCS-like s -wave state. Consequently, the leading pairing tendency is driven by spin fluctuations in the vicinity of the spin-density-wave instability.

In the static approximation, we set $\mathcal{V}_{s/t}(\mathbf{p}, i\omega_n - i\omega_m) \approx \mathcal{V}_{s/t}(\mathbf{p})$ and $\Delta_{s/t}(\mathbf{k}, i\omega_n) \approx \Delta_{s/t}(\mathbf{k})$. Carrying out the resulting Matsubara sum then reduces Eq. (12) to

the well-known static, finite-temperature mean-field gap equation reported in Supplementary Material Sec. S3B. In this work, we focus on the paramagnetic regime: we determine U_{eff} and solve the corresponding gap equations in both the spin-singlet and spin-triplet channels. For the numerical solution, we discretize the Brillouin zone by sampling $\mathbf{k} = (k_x, k_y)$ with $k_{x,y} \in [0, 2\pi)$, chosen such that in the continuum limit the resulting \mathbf{k} -sums converge to properly normalized Brillouin-zone integrals. To capture the leading pairing symmetries, we introduce a set of real form factors $\{\varphi_\alpha(\mathbf{k})\}$ (Supplementary Sec. S4) and expand the gap as

$$\Delta(\mathbf{k}, i\omega_n) = \sum_{\alpha} c_{\alpha}(i\omega_n) \varphi_{\alpha}(\mathbf{k}), \quad (13)$$

with complex coefficients $c_{\alpha}(i\omega_n)$ determined self-consistently (see Supplemental Material, Sec. S4C). The dominant pairing symmetry is identified from the largest weight at the lowest Matsubara frequency, $i\omega_0 = i\pi T$. Using the orthonormality condition

$$\int_{\text{BZ}} \frac{d^2k}{(2\pi)^2} \varphi_{\alpha}^*(\mathbf{k}) \varphi_{\beta}(\mathbf{k}) = \delta_{\alpha\beta}, \quad (14)$$

the gap norm at $i\omega_0$ becomes

$$\begin{aligned} \|\Delta(i\omega_0)\|^2 &= \int_{\text{BZ}} \frac{d^2k}{(2\pi)^2} \Delta^\dagger(\mathbf{k}, i\omega_0) \Delta(\mathbf{k}, i\omega_0) \\ &= \sum_{\alpha} |c_{\alpha}(i\omega_0)|^2. \end{aligned} \quad (15)$$

Accordingly, the leading pairing channel is the one with the largest contribution to $\|\Delta(i\omega_0)\|$. So this gap amplitude provides a compact, gauge-independent measure of the total superconducting amplitude across all symmetry channels.

III. RESULTS

A. Spin/charge fluctuation landscape

We analyze the spin susceptibilities and Fermi surface landscape across the full doping range for a next-nearest-neighbor hopping $t' = -0.2$ motivated by the cuprate Fermiology [50], where we mainly focus on the hole-doping. The zero-frequency limit $\chi_{s/c}(\mathbf{q}, i\Omega_0)$ provides a compact measure of the low-energy fluctuation landscape: peaks of $\chi_s(\mathbf{q})$ identify the wave vectors at which magnetic correlations are strongest and, in spin-fluctuation pairing scenarios, indicate the dominant momentum transfers that enter the effective pairing interaction [15, 51, 52]. While a fully dynamical treatment is required for quantitative Eliashberg analysis, the static spectrum is widely used as a transparent approximation and a guide to pairing intuition, because it already captures how the relevant scattering channels evolve with filling [21, 51, 53, 54].

Fig. 1 summarizes the evolution of the static fluctuation spectrum across the corresponding filling range. The first three rows (Fig. 1a-1i) show the static ($i\Omega_0$) spin susceptibility $\chi_s(\mathbf{q})$, charge $\chi_c(\mathbf{q})$, and the bare susceptibility/Lindhard bubble $\chi_0(\mathbf{q})$, while the last row displays the corresponding Fermi surfaces and the projected nodal features of the leading SC gap, derived by solving the dynamic gap equation as delineated above. At low filling ($n \lesssim 0.4$), both χ_s and χ_c display their strongest intensity near the zone boundaries at $(\pm\pi, 0)$ and $(0, \pm\pi)$, consistent with dominant particle-hole scattering across a small electron-like Fermi surface. As n increases, these maxima gradually shift away from the high-symmetry points and evolve into the characteristic quartet of incommensurate peaks at $(\pi \pm \delta, \pi)$ and $(\pi, \pi \pm \delta)$ [47, 55], signaling the development of increasingly well-nested wave vectors and the approach to nearly perfect nesting as the Fermi surface expands. Close to half-filling, the response sharpens and becomes strongly concentrated around $\mathbf{q} = (\pi, \pi)$, reflecting the enhancement of commensurate antiferromagnetic correlations. Throughout this evolution, the charge channel remains comparatively weak and only weakly structured, indicating that the pairing-relevant interaction is predominantly mediated by spin fluctuations.

This evolution of the Fermi surface underlies the momentum-resolved spin and charge responses discussed above and is shown in the bottom row of Fig. 1. For low densities ($n \lesssim 0.4$), the Fermi surface forms a small, nearly circular electron-like pocket centred at Γ , such that the dominant particle-hole scattering arises from

momenta connecting opposite sides of this pocket. With increasing filling, the Fermi surface expands toward the Brillouin-zone boundary and progressively develops flatter segments. At the Van Hove filling (for $t' = -0.2$, this occurs near $n_{\text{vH}} \simeq 0.83$), the Fermi surface touches the saddle points at $(\pm\pi, 0)$ and $(0, \pm\pi)$. Beyond this Lifshitz point, the topology becomes hole-like with a large Fermi surface centered around (π, π) ; the emergence of extended, nearly parallel segments enhances the phase space for near-nesting scattering and tends to promote incommensurate wave vectors in the spin response.

B. n - U Phase diagrams

We chart the leading superconducting instability as a function of density n and interaction strength U at fixed $t' = -0.2$ and $T = 0.02t$, using the dynamical fluctuation-mediated pairing vertices of Eqs. 10–9. For each (n, U) , we construct $\mathcal{V}_{s/t}(q)$ from the slave-boson susceptibilities, project the nonlinear gap equation onto the chosen form-factor basis, and identify the leading solution from the form factor with the largest low-frequency weight. Since the gap equation is nonlinear, we converge to a unique solution via self-consistent iteration on the projected basis. The intermediate-representation basis and the sparse sampling of imaginary-time and Matsubara-frequency quantities are implemented using the `sparse-ir` library [56].

Fig. 2(a) depicts the singlet SC phase diagram from Ref. [43], including the transition line between the magnetically ordered phase (white region). Three distinct regions appear: (I) a mixed $d_{xy} + d_{xy}^{(2)}$ state at low fillings, which persists up to $n \simeq 0.35$ even for large U ; at low filling, broad spin susceptibility peaks near $(\pm\pi, 0)$ and $(0, \pm\pi)$ drive scattering of the nearly circular Fermi-surface segments beyond the first-harmonic form factor. The higher-order admixture $d_{xy}^{(2)} \propto (\sin k_x \sin 2k_y + \sin 2k_x \sin k_y)$ adds nodes that better match these transfers on the small, near-circular Fermi surface (Fig. 1). (II) a pure $d_{xy} \propto \sin k_x \sin k_y$ regime at intermediate fillings; and (III) a $d_{x^2-y^2}$ region toward higher n , with a clear $d_{xy} \rightarrow d_{x^2-y^2}$ transition near $n \simeq 0.61$. The evolution of the dominant pairing symmetry closely follows the structure of the spin susceptibility $\chi_s(\mathbf{q})$ in Fig. 1: when the AF-enhanced wave vectors connect Fermi-surface regions where candidate d -wave form factors have opposite signs, those d -wave channels are selected, with the competition between d_{xy} and $d_{x^2-y^2}$ determined by the Fermi-surface geometry and the location of the spin-response maxima. This global pattern is quantitatively consistent with weak to intermediate coupling RPA studies and with constrained-path QMC benchmarks, both in terms of the assigned pairing symmetry and in the approximate position of the d_{xy} - $d_{x^2-y^2}$ boundary [3, 18, 47]. We directly compare our results with the RPA-predicted critical interaction (U_c) in the spin channel in Fig. 2(a). Since RPA retains only

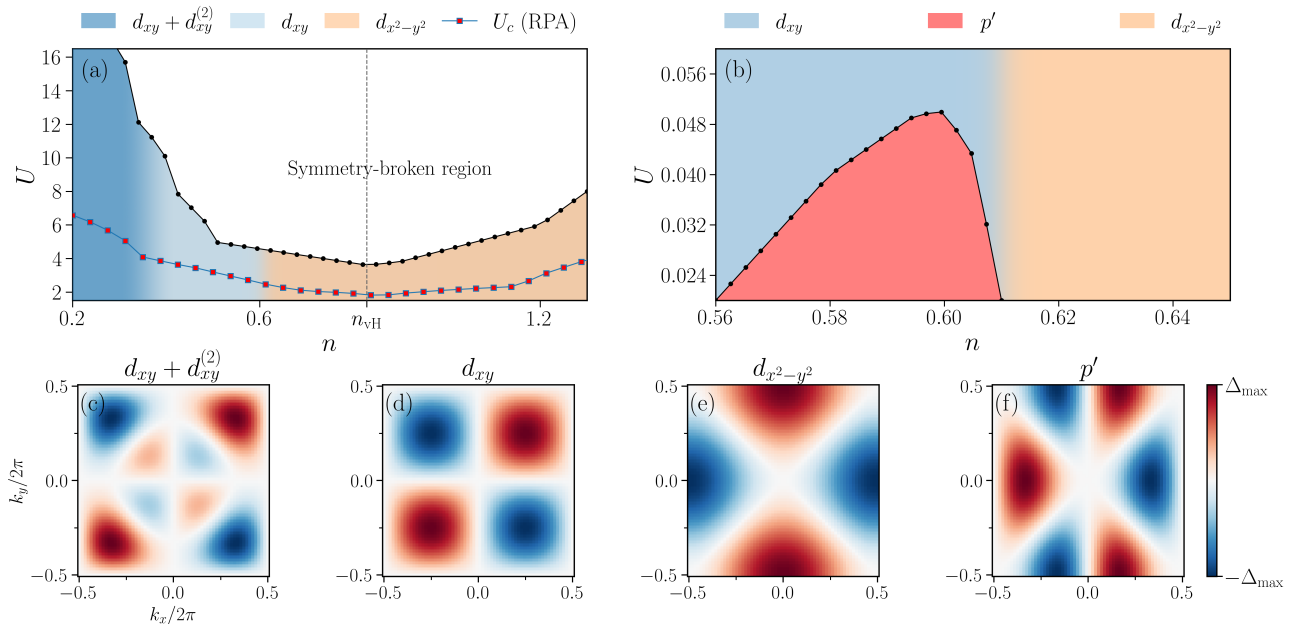


FIG. 2. n - U phase diagrams at $T = 0.02t$. (a) Paramagnetic-state superconducting phase diagram; color encodes the leading instability. The $d_{xy} + d_{xy}^{(2)}$ state persists up to $n \simeq 0.35$ even at large U , and a $d_{xy} \rightarrow d_{x^2-y^2}$ transition occurs near $n \simeq 0.61$. The overall phase diagram agrees with weak–intermediate coupling RPA results [18, 47] and CPQMC simulations [3]. (b) Phase diagram at lower U showing the leading instability including the triplet p' phase (for $T = 0.01t$). The p' state belongs to the E_u irreducible representation and corresponds to a six-node triplet solution, consistent with [48, 49]. (c)–(f) Representative gap structures in \mathbf{k} space for $d_{xy} + d_{xy}^{(2)}$, d_{xy} , $d_{x^2-y^2}$, and p' respectively. Red markers indicate the RPA-predicted critical interaction (U_c) in the spin channel. The van-Hove filling is indicated by a violet dashed line at $n_{vH} = 0.83$.

particle–hole ladder diagrams and neglects other scattering channels, it typically underestimates the overall critical scale, particularly at dopings far from the Van Hove singularity[57]. Fig. 2(b) reveals a narrow p' region situated in the transition zone between the d_{xy} and $d_{x^2-y^2}$ sectors. At lower U , this region coincides with the dominance of the triplet channel. The p' state belongs to the E_u irreducible representation and is spanned by two degenerate basis functions, of which we show only one; the other is obtained by a 90-degree rotation and has a node along the k_x axis. On the Fermi surface, this state displays a six-node structure, consistent with earlier diagrammatic Monte Carlo and FLEX+RPA results [47, 48]. Fig. 2(c–f) illustrates the representative gap structures in momentum space. Notably, the p' gap function shares nodes with both neighboring d -wave states, making it a consistent intermediate solution at the phase boundary where the transition is near $U = 0$.

We emphasize that the large- U part of the depicted phase diagram should be viewed primarily as theory space for internal consistency checks and for classifying pairing tendencies within the model, rather than as a directly material-motivated regime.

C. Filling dependence of fluctuation & pairing scale

The momentum-resolved susceptibilities in Fig. 1 can be summarized by two filling-dependent quantities entering the pairing kernel: (i) the overall magnitude of magnetic fluctuations, quantified by the peak value of the static spin susceptibility, $\max_{\mathbf{q}} \chi_s(\mathbf{q}, i\Omega_0)$, and (ii) the effective interaction scale $U_{\text{eff}}(n)$ extracted at the dominant magnetic wave vector \mathbf{Q} (Sec. II A). Although the pairing kernel receives contributions from higher bosonic Matsubara frequencies, its qualitative behavior is largely determined by the lowest bosonic frequency, which typically carries the dominant weight. Fig. 3(a,b) depicts both quantities for representative interactions $U = 1, 2$, with background shading indicating the leading singlet symmetry regions from Fig. 2.

As shown in Fig. 3(a), the magnetic response is weak at low filling ($n \lesssim 0.35$), where the system resides in the $d_{xy} + d_{xy}^{(2)}$ sector and χ_s remains small and only weakly varying with n . Upon entering the intermediate-density d_{xy} regime, $\max_{\mathbf{q}} \chi_s$ increases more noticeably, consistent with the development of stronger near-nesting scattering channels and the progressive sharpening of the spin response seen in Fig. 1. The most pronounced enhancement occurs in the $d_{x^2-y^2}$ sector ($n \gtrsim 0.61$): for $U = 2$ the maximal static susceptibility rises rapidly and forms a dome near the high-filling end, signalling prox-

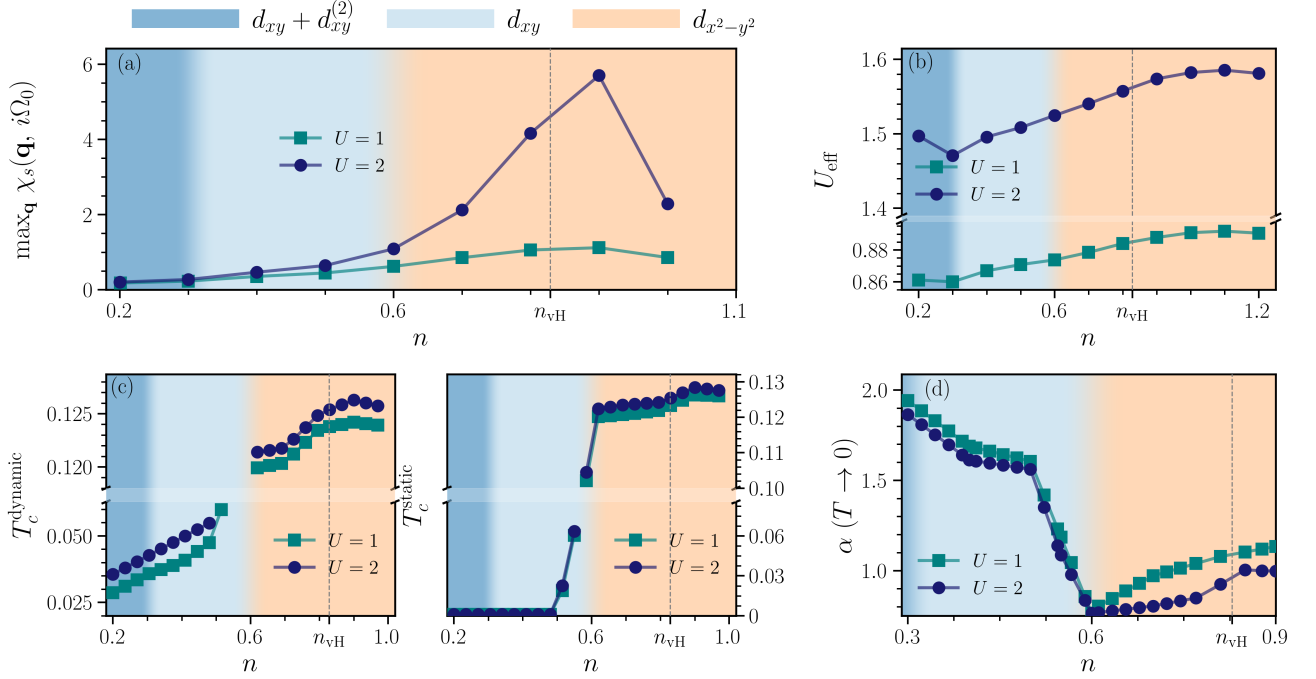


FIG. 3. Filling dependence of magnetic response, effective interaction scale, and superconducting properties. (a) Maximum static spin susceptibility $\max_{\mathbf{q}} \chi_s(\mathbf{q}, i\Omega_0)$ versus filling n for $U = 1$ and $U = 2$. (b) Effective interaction scale U_{eff} determined by matching the Stoner-enhanced $\chi_s(\mathbf{Q})$ to an RPA form at the dominant wave vector \mathbf{Q} ; axis break indicates the different magnitude for $U = 1$ and $U = 2$. (c) Estimated critical temperatures obtained from the full frequency-dependent (dynamic) gap equation (left) and from the static approximation (right); (d) Exponent α characterizing the decay of the Matsubara-axis gap, $\Delta(i\omega_n) \sim |\omega_n|^{-\alpha}$, shown as a function of n . Background shading indicates the leading singlet symmetry region ($d_{xy} + d_{xy}^{(2)}$, d_{xy} , $d_{x^2-y^2}$), and the vertical dashed line marks the van Hove filling n_{vH} .

imity to a Stoner-enhanced antiferromagnetic instability. For $U = 1$ the increase is more modest but follows the same monotonic trend, indicating that the strengthening of magnetic fluctuations with filling is a robust feature even at weaker couplings. The vertical dashed line marks the van Hove filling n_{vH} ; across this point, the magnetic response continues to grow, consistent with an enhanced phase space for particle-hole scattering and the associated amplification of spin fluctuations.

The extracted $U_{\text{eff}}(n)$ in Fig. 3(b) provides a compact interaction scale that enters the fluctuation-exchange vertices of Eqs. (10)–(9). By construction, U_{eff} is determined from the ratio between the interacting and bare responses at the dominant wave vector \mathbf{Q} , and therefore tracks the degree of Stoner enhancement encoded in $\chi_s(\mathbf{Q})$. For both $U = 1$ and $U = 2$, U_{eff} increases smoothly with filling, reflecting the systematic strengthening of magnetic correlations as the system moves toward the high-filling $d_{x^2-y^2}$ regime. We find that U_{eff} scales approximately linearly with U , and that its renormalization with filling is stronger at larger U . Together, Figs. 3(a) and 3(b) therefore quantify the two central ingredients for pairing: the buildup of spin-fluctuation spectral weight and the resulting enhancement of the effective interaction scale that sets the overall strength of the pairing vertex. Below, we relate these trends to the evolution of the dynamical gap

structure and the resulting T_c .

D. Critical Temperature T_c

We extract the superconducting critical temperature T_c from temperature sweeps of the fully self-consistent solutions of the gap equation, using the gap amplitude defined by the Brillouin-zone norm in Eq. (15); T_c is identified as the highest temperature at which a nontrivial solution persists. Fig. 3(c) compares T_c obtained from the full frequency-dependent (dynamic) gap equation, T_c^{dynamic} , with the static approximation, T_c^{static} , for representative interactions $U = 1, 2$. In the high-filling $d_{x^2-y^2}$ regime, where the magnetic response is strongest, T_c^{static} systematically exceeds T_c^{dynamic} : treating the pairing kernel as instantaneous effectively weights the interaction by its $\Omega = 0$ component over the full frequency spectrum and therefore overestimates the pairing strength, while the dynamic equation includes the full Ω dependence of the spin/charge fluctuations entering the vertex, which reduces the net pairing efficiency and suppresses T_c through retardation and fluctuation-induced scattering encoded in $\mathcal{V}_{s/t}(\mathbf{p}, i\Omega_{nm})$.

The doping dependence of T_c closely tracks the evolution of the spin fluctuations: $\max_{\mathbf{q}} \chi_s(\mathbf{q}, i\Omega_0)$ grows

strongly upon approaching the $d_{x^2-y^2}$ region [Fig. 3(a)], and at the same time both U_{eff} [Fig. 3(b)] and T_c are enhanced, consistent with spin-fluctuation-dominated pairing [58]. By contrast, at low fillings, *i.e.* in the $d_{xy} + d_{xy}^{(2)}$ and d_{xy} regimes, the spin response is weaker and broader in momentum space, yielding substantially smaller T_c in both the static and dynamic treatments. Intuitively, the dynamic transition typically exceeds the static one, reflecting the fact that the full frequency dependence of the pairing kernel allows pairing to persist at higher temperatures than the zero-frequency approximation, even when the static Stoner enhancement is weak. In this regime, the reduced Stoner enhancement and less favorable scattering geometry limit the effective pairing scale in the static limit, whereas the dynamic equation accesses weight away from small frequencies and can support a finite solution at somewhat higher T_c (see also Supplementary Material Fig. S4.5). This is consistent with experimental expectations in cuprate systems, where accessible superconductivity emerges primarily at higher fillings and not at the low-doping end of the phase diagram; the strong suppression of T_c at low fillings indicates that unconventional superconductivity is unlikely to be observed in this regime, given typical experimental sensitivity and sample-quality requirements.

Notably, the estimated $T_c(n)$ peaks away from the van Hove filling n_{vH} (Fig. 3(c)), qualitatively aligning with cuprate experiments where optimal hole-doping precedes the van-Hove singularity [59–62], though our generic model eschews material-specific predictions. As we will point out in the following sections the real-frequency gap $\Re\Delta(\omega)$ exhibits a dynamical softening with increasing n (Supp. Fig. S4.4): a pronounced low-energy peak structure $\omega_{\text{peak}}(n)$ reduces with increasing filling. Such a feature naturally identifies the characteristic (retarded) scale of the effective pairing glue provided by spin fluctuations. In realistic materials, stronger retardation may amplify this feedback, raising T_c beyond our RPA-like estimates [20, 63].

E. Frequency dependent Gap profile

Matsubara-axis solutions of the full (dynamic) gap equation provide direct access to the frequency structure of the superconducting order parameter. The analysis starts from discrete data $\{z_n = i\omega_n, \Delta(i\omega_n)\}$ obtained from the self-consistent solver, where $\Delta(i\omega_n)$ is evaluated at a representative momentum on the Fermi surface. The large- $|\omega_n|$ tail is well described by a power law, $\Delta(i\omega_n) \sim |\omega_n|^{-\alpha}$ so that the exponent α provides a compact characterization of the retardation contained in the fluctuation-mediated pairing kernel.

The filling dependence of α is summarized in Fig. 3(d). In the $d_{x^2-y^2}$ regime, values $\alpha \sim 1$ indicate a slowly decaying gap tail, consistent with pairing dominated by strong antiferromagnetic fluctuations. By contrast, the larger α values in the low-density d_{xy} sector correspond

to a more rapidly decaying gap response, suggesting a less strongly retarded effective pairing kernel (Supplementary Material Fig. S4.5). A pronounced reduction of α occurs near the symmetry-changing boundary, signalling enhanced low-frequency pairing fluctuations associated with competition between nearly degenerate d_{xy} and $d_{x^2-y^2}$ channels. This behavior is naturally connected to quantum-critical pairing scenarios such as Chubukov’s γ -model, where a singular bosonic glue $\lambda(\Omega_m) \propto 1/|\Omega_m|^\gamma$ can generate power-law Matsubara-frequency structures over an extended scaling window [64, 65]. The same dynamical structure is also reflected in the systematic suppression of the dynamic critical temperature relative to the static approximation discussed in Fig. 3(c).

While $\Delta(i\omega_n)$ is the natural output of the dynamical gap equation, identifying characteristic pairing scales requires access to the real-frequency gap $\Delta(\omega)$. Since the momentum dependence has already been separated into the form-factor expansion of Eq. (13), we can isolate the frequency dependence by integrating out the momentum dependence and are left with a purely frequency-dependent function $\Delta(i\omega_n)$. In practice, it is often simplest to select a single representative momentum \mathbf{k}^* and use this point to iterate the frequency dependence; the extracted behavior turns out to describe the entire momentum spectrum accurately, which reinforces the validity of our product ansatz in Eq. (13). Notably, some studies suggest [66, 67] that there can be a nontrivial intertwining of the functional spaces in (\mathbf{k}, ω) , but in our case such coupling appears to be weak. Methodologically, however, our approach does not hinge on the product ansatz and can be generalized beyond it.

Because analytic continuation is numerically demanding and not generally feasible, we construct an analytic approximation $\Delta(z)$ from the Matsubara-axis data using an N -point Padé approximant $P_N(z)$ in the continued-fraction form [68, 69] (see Supplementary Sec. S5),

$$\Delta(\omega) = \lim_{\eta \rightarrow 0^+} P_N(\omega + i\eta). \quad (16)$$

Analytic continuation is here more straightforward: for $\omega > 0$, the resulting $\Re\Delta(\omega)$ is well described by a minimal phenomenological form that captures both a pronounced finite-frequency structure around a characteristic scale ω_p and a slowly decaying high-frequency tail,

$$\Re\Delta(\omega) = c_0 + C \frac{\omega - \omega_p}{(\omega - \omega_p)^2 + \Gamma^2} + \frac{1}{A + B\omega^\lambda}. \quad (17)$$

The constant offset c_0 is retained to improve the numerical stability of the fit and to absorb small residual offsets from the Padé continuation; in practice, however, we find c_0 to be negligible in subsequent analysis. The second term is dispersive in the sense that it describes a resonant, frequency-dependent correction with a non-constant spectral shape. On its own, this term corresponds to a Lorentzian-like response in the time domain, reflecting the finite lifetime and oscillatory decay of the underlying fluctuation mode. The last term reproduces

the algebraic tail already visible on the Matsubara axis. The corresponding fits for both $\Re\Delta(\omega)$ and $\Im\Delta(\omega)$ are shown in Supplementary Fig. S4.4. The imaginary part is not fitted independently. Instead, it is constrained by causality and obtained from the Kramers–Kronig relation,

$$\Im\Delta(\omega) = -\frac{1}{\pi} \mathcal{P} \int_{-\infty}^{\infty} \frac{\Re\Delta(\omega')}{\omega' - \omega} d\omega', \quad (18)$$

$$\Re\Delta(\omega) = \frac{1}{\pi} \mathcal{P} \int_{-\infty}^{\infty} \frac{\Im\Delta(\omega')}{\omega' - \omega} d\omega'. \quad (19)$$

This procedure yields excellent agreement for $\Im\Delta(\omega)$ and provides a stringent consistency check on the real-axis continuation. The fit also makes the limiting behavior transparent:

$$\Re\Delta(\omega \rightarrow 0) = -C \frac{\omega_p}{\omega_p^2 + \Gamma^2} + \frac{1}{A}, \quad (20)$$

At low filling, the real-frequency gap function is well described by a purely dispersive form, whereas at higher filling, an additional broad tail is required to accurately capture the data over the accessible frequency window. The dispersive part decays as $1/\omega$ for large ω , while the tail contributes a correction $\sim \omega^{-\lambda}$. For the stable high-filling fits we find $\lambda > 1$, implying that this tail is subleading in the $\omega \rightarrow \infty$ limit. Our parametrization captures both the characteristic intermediate-frequency structure and the subleading power-law correction visible in Supplementary Fig. S4.4, while leaving the leading asymptotic behavior consistent. This interpretation is consistent with earlier studies reporting enhanced finite-frequency structure in dynamical gap functions, although without showing an explicit fitting framework [20, 65, 68, 70, 71].

Upon Padé continuation, $\Re\Delta(\omega)$ develops a pronounced finite-frequency peak whose position $\omega_{\text{peak}}(n)$ and magnitude evolve systematically with filling. We extract ω_{peak} from the fit in Eq. (17) and find the same qualitative trend when comparing the slave-boson results to FLEX+RPA at the same (U, t') (Supplementary Fig. S4.6). As n increases, ω_{peak} shifts to lower frequencies and exhibits a clear change in slope near the $d_{xy} \rightarrow d_{x^2-y^2}$ crossover.

Since the momentum dependence is already encoded in the form-factor expansion, this trend reflects how the leading pairing channel samples different parts of the spin-fluctuation spectrum as the filling is varied. In the language of spin-fluctuation pairing, the downward shift of ω_{peak} indicates a softening of the characteristic energy scale of the effective pairing interaction, i.e. the dominant spectral weight of the pairing glue moves to lower frequencies near half filling [20, 21, 66, 67]. The overall trend is broadly consistent with experiment, in $\text{Bi}_2\text{Sr}_2\text{CaCu}_2\text{O}_{8+\delta}$, high-resolution ARPES revealed clear superconductivity-induced changes in the near-nodal electronic excitations [72]. Subsequent measurements on overdoped Bi2212 showed that the renormalization weakens with doping and disappears together

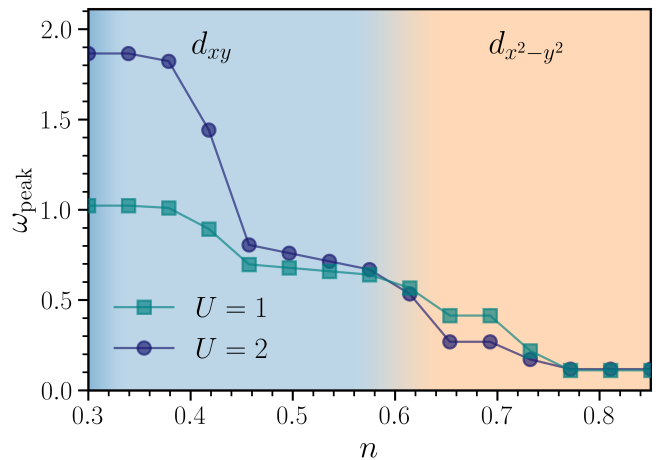


FIG. 4. Filling dependence of the real-frequency gap peak scale. Peak position ω_{peak} of $\Re\Delta(\omega)$, extracted from the Padé-continued gap using the fit form in Eq. (17), shown as a function of filling n for $t' = -0.2$ and $U = 1, 2$. Background shading indicates the leading singlet symmetry regions from Fig. 2. With increasing filling, ω_{peak} shifts systematically to lower frequencies and shows a clear change in slope across the $d_{xy} \rightarrow d_{x^2-y^2}$ crossover.

with superconductivity, identifying the onset of the spin-fluctuation spectrum as the relevant low-energy scale [73]. In this sense, the reduction of ω_{peak} with increasing filling in our calculation can be viewed as a signature of the same softening tendency in the characteristic electronic renormalization scale [74, 75].

IV. CONCLUSION

We have developed a superconducting fluctuation-exchange framework within the spin-rotation-invariant Kotliar–Ruckenstein slave-boson formulation of the two-dimensional Hubbard model with t – t' hopping. Starting from Gaussian fluctuations about the paramagnetic saddle point, we obtained fully dynamical spin and charge susceptibilities built on a correlated Gutzwiller-renormalized quasiparticle background. This correlated starting point distinguishes the present approach from weak-coupling fluctuation-exchange schemes based on bare quasiparticles, since strong-correlation renormalizations enter already at the level of the quasiparticle dispersion and collective susceptibilities. These susceptibilities were then used to construct an effective two-particle pairing vertex that is explicitly antisymmetric under fermionic exchange and can be decomposed into singlet and triplet channels. Solving the resulting anisotropic, frequency-dependent gap equation in a form-factor basis allowed us to map the leading superconducting instabilities over filling and interaction strength and to access both Matsubara- and real-frequency properties of the gap.

The central physical result is that pairing is dominated throughout by the spin-fluctuation channel. In the paramagnetic regime studied here, the leading singlet symmetry evolves systematically from a low-filling $d_{xy} + d_{xy}^{(2)}$ state to an intermediate d_{xy} regime and finally to a high-filling $d_{x^2-y^2}$ state. This sequence closely follows the filling-dependent evolution of $\chi_s(\mathbf{q})$ and the corresponding dominant scattering wave vectors, consistent with the standard sign-changing spin-fluctuation mechanism. At the same time, both the maximal static spin response and the interaction scale U_{eff} extracted from the Stoner enhancement grow toward higher filling, leading to an enhancement of the pairing scale and of the estimated T_c . While the low-filling sectors are useful for classifying the intrinsic pairing tendencies of the model theoretically, the higher-filling $d_{x^2-y^2}$ regime connects more directly to the parameter range usually associated with cuprate phenomenology.

The dynamical gap structure provides additional information beyond the symmetry classification. On the Matsubara axis, the gap shows a robust power-law decay $\Delta(i\omega_n) \sim |\omega_n|^{-\alpha}$ with a filling-dependent exponent, and the fully dynamic calculation yields systematically lower critical temperatures than the static approximation for the high-filling regime, demonstrating the importance of retardation effects. After Padé continuation, the real part of the gap develops a pronounced finite-frequency peak whose position ω_{peak} shifts to lower energies with increasing filling and changes slope near the d_{xy} to $d_{x^2-y^2}$ crossover. We interpret this as a dynamical fingerprint of the softening of the characteristic pairing scale encoded in the spin-fluctuation spectrum. In this sense, the real-

frequency analysis provides a direct way to characterize how the effective pairing glue evolves across the phase diagram.

Several extensions of the present approach suggest themselves and provide a roadmap for future work. On the methodological side, it would be valuable to incorporate additional self-energy feedback beyond the current quasiparticle renormalization, to capture the back-action of superconductivity on the fluctuation spectrum and to allow for competing symmetry-broken states beyond the paramagnetic saddle, such as magnetic or charge order. Extending the framework to multi-orbital settings would further pave the way toward more material-specific applications. More broadly, the present work establishes a scalable route from slave-boson fluctuation dynamics to microscopic pairing interactions, superconducting phase competition, and dynamical gap properties in correlated lattice systems, which can serve as a basis for such future refinements.

V. ACKNOWLEDGEMENT

We thank T. Saha-Dasgupta, I. Dasgupta, M. Dürrnagel, L. Klebl and T. Müller for fruitful discussions. This research was funded by the Deutsche Forschungsgemeinschaft (DFG, German Research Foundation) – Project-ID 258499086 – SFB 1170; through the Würzburg-Dresden Cluster of Excellence on Complexity, Topology, and Dynamics in Quantum Materials (ctd.qmat) – Project-ID 390858490 – EXC 2147; P. Wölfle acknowledges support through a Distinguished Senior Fellowship of Karlsruhe Institute of Technology.

-
- [1] R. Blankenbecler, D. J. Scalapino, and R. L. Sugar, Monte carlo calculations of coupled boson-fermion systems. i, *Physical Review D* **24**, 2278 (1981).
 - [2] S. Zhang, J. Carlson, and J. E. Gubernatis, Pairing correlations in the two-dimensional hubbard model, *Physical Review Letters* **78**, 4486 (1997).
 - [3] Z. Cao, J. Li, J. Su, T. Ying, and H.-K. Tang, Dominant p -wave pairing induced by nearest-neighbor attraction in the square-lattice extended hubbard model, *Physical Review B* **111**, 024509 (2025).
 - [4] S. R. White, Density matrix formulation for quantum renormalization groups, *Physical Review Letters* **69**, 2863 (1992).
 - [5] S. R. White and D. J. Scalapino, Stripes on a 6-leg hubbard ladder, *Physical Review Letters* **91**, 136403 (2003).
 - [6] Y.-F. Jiang, T. P. Devereaux, and H.-C. Jiang, Ground-state phase diagram and superconductivity of the doped hubbard model on six-leg square cylinders, *Physical Review B* **109**, 085121 (2024).
 - [7] G. Knizia and G. K.-L. Chan, Density matrix embedding: A simple alternative to dynamical mean-field theory, *Physical Review Letters* **109**, 186404 (2012).
 - [8] B.-X. Zheng and G. K.-L. Chan, Ground-state phase diagram of the square lattice hubbard model from density matrix embedding theory, *Physical Review B* **93**, 035126 (2016).
 - [9] R. Shankar, Renormalization-group approach to interacting fermions, *Reviews of Modern Physics* **66**, 129 (1994).
 - [10] C. J. Halboth and W. Metzner, d -wave superconductivity and pomeranchuk instability in the two-dimensional hubbard model, *Physical Review Letters* **85**, 5162 (2000).
 - [11] C. Honerkamp and M. Salmhofer, Magnetic and superconducting instabilities of the hubbard model at the van hove filling, *Physical Review Letters* **87**, 187004 (2001).
 - [12] W. Metzner, M. Salmhofer, C. Honerkamp, V. Meden, and K. Schönhammer, Functional renormalization group approach to correlated fermion systems, *Reviews of Modern Physics* **84**, 299 (2012).
 - [13] W. Kohn and J. M. Luttinger, New mechanism for superconductivity, *Physical Review Letters* **15**, 524 (1965).
 - [14] J. M. Luttinger, New mechanism for superconductivity, *Physical Review* **150**, 202 (1966).
 - [15] N. F. Berk and J. R. Schrieffer, Effect of ferromagnetic spin correlations on superconductivity, *Physical Review Letters* **17**, 433 (1966).

- [16] D. J. Scalapino, E. Loh, and J. E. Hirsch, d -wave pairing near a spin-density-wave instability, *Physical Review B* **34**, 8190 (1986).
- [17] D. J. Scalapino, The case for $d_{x^2-y^2}$ pairing in the cuprate superconductors, *Physics Reports* **250**, 329 (1995).
- [18] A. T. Rømer, A. Kreisel, I. Eremin, M. A. Malakhov, T. A. Maier, P. J. Hirschfeld, and B. M. Andersen, Pairing symmetry of the one-band hubbard model in the paramagnetic weak-coupling limit: A numerical RPA study, *Physical Review B* **92**, 104505 (2015).
- [19] F. I. V. Šimkovic, X.-W. Liu, Y. Deng, and E. Kozik, Ground-state phase diagram of the repulsive fermionic hubbard model on the square lattice from weak coupling, *Physical Review B* **94**, 085106 (2016).
- [20] P. Monthoux and D. J. Scalapino, Self-consistent $d_{x^2-y^2}$ pairing in a two-dimensional hubbard model, *Physical Review Letters* **72**, 1874 (1994).
- [21] N. E. Bickers, D. J. Scalapino, and S. R. White, Conserving approximations for strongly correlated electron systems: Bethe-Salpeter equation and dynamics for the two-dimensional hubbard model, *Physical Review Letters* **62**, 961 (1989).
- [22] W. Metzner and D. Vollhardt, Correlated lattice fermions in $d = \infty$ dimensions, *Phys. Rev. Lett.* **62**, 324 (1989).
- [23] A. Georges and G. Kotliar, Hubbard model in infinite dimensions, *Phys. Rev. B* **45**, 6479 (1992).
- [24] A. Georges, G. Kotliar, W. Krauth, and M. J. Rozenberg, Dynamical mean-field theory of strongly correlated fermion systems and the limit of infinite dimensions, *Rev. Mod. Phys.* **68**, 13 (1996).
- [25] K. Held, Electronic structure calculations using dynamical mean field theory, *Advances in Physics* **56**, 829 (2007), <https://doi.org/10.1080/00018730701619647>.
- [26] G. Rohringer, H. Hafermann, A. Toschi, A. A. Katani, A. E. Antipov, M. I. Katsnelson, A. I. Lichtenstein, A. N. Rubtsov, and K. Held, Diagrammatic routes to nonlocal correlations beyond dynamical mean field theory, *Rev. Mod. Phys.* **90**, 025003 (2018).
- [27] M. C. Gutzwiller, Effect of correlation on the ferromagnetism of transition metals, *Physical Review Letters* **10**, 159 (1963).
- [28] M. C. Gutzwiller, Effect of correlation on the ferromagnetism of transition metals, *Physical Review* **134**, A923 (1964).
- [29] M. C. Gutzwiller, Correlation of electrons in a narrow s band, *Physical Review* **137**, A1726 (1965).
- [30] W. F. Brinkman and T. M. Rice, Application of gutzwiller's variational method to the metal-insulator transition, *Physical Review B* **2**, 4302 (1970).
- [31] D. Vollhardt, Normal ^3He : An almost localized fermi liquid, *Reviews of Modern Physics* **56**, 99 (1984).
- [32] G. Kotliar and A. E. Ruckenstein, New functional integral approach to strongly correlated fermi systems: The gutzwiller approximation as a saddle point, *Physical Review Letters* **57**, 1362 (1986).
- [33] R. Frésard and G. Kotliar, Interplay of mott transition and ferromagnetism in the orbitally degenerate hubbard model, *Physical Review B* **56**, 12909 (1997).
- [34] F. Lechermann, A. Georges, G. Kotliar, and O. Parcollet, Rotationally invariant slave-boson formalism and momentum dependence of the quasiparticle weight, *Physical Review B* **76**, 155102 (2007).
- [35] M. Legner, A. Rüegg, and M. Sigrist, Topological invariants, surface states, and interaction-driven phase transitions in correlated kondo insulators with cubic symmetry, *Phys. Rev. B* **89**, 085110 (2014).
- [36] M. Klett, S. Ok, D. Riegler, P. Wölfle, R. Thomale, and T. Neupert, Topology and magnetism in the kondo insulator phase diagram, *Phys. Rev. B* **101**, 161112 (2020).
- [37] J. Hubbard, Electron correlations in narrow energy bands, *Proceedings of the Royal Society of London. Series A* **276**, 238 (1963).
- [38] J. Kanamori, Electron correlation and ferromagnetism of transition metals, *Progress of Theoretical Physics* **30**, 275 (1963).
- [39] P. W. Anderson, The resonating valence bond state in La_2CuO_4 and superconductivity, *Science* **235**, 1196 (1987).
- [40] F. C. Zhang and T. M. Rice, Effective hamiltonian for the superconducting cu oxides, *Physical Review B* **37**, 3759 (1988).
- [41] T. Li, Y. S. Sun, and P. Wölfle, Dynamic response functions of Hubbard model in Gutzwiller approximation, *Z. Physik B - Condensed Matter* **82**, 369 (1991).
- [42] W. Zimmermann, R. Frésard, and P. Wölfle, Spin and charge structure factor of the two-dimensional hubbard model, *Physical Review B* **56**, 10097 (1997).
- [43] D. Riegler, M. Klett, T. Neupert, R. Thomale, and P. Wölfle, Slave-boson analysis of the two-dimensional hubbard model, *Physical Review B* **101**, 235137 (2020).
- [44] J. Seufert, D. Riegler, M. Klett, R. Thomale, and P. Wölfle, Breakdown of charge homogeneity in the two-dimensional hubbard model: Slave-boson study of magnetic order, *Physical Review B* **103**, 165117 (2021).
- [45] M. Pfitzner and P. Wölfle, Quasiparticle interaction in a nearly localized fermi liquid: Application to liquid He_3 and heavy-fermion systems, *Physical Review B* **33**, 2003 (1985).
- [46] G. M. Eliashberg, Interactions between electrons and lattice vibrations in a superconductor, *Sov. Phys. JETP* **11**, 696 (1960).
- [47] A. T. Rømer, T. A. Maier, A. Kreisel, I. Eremin, P. J. Hirschfeld, and B. M. Andersen, Pairing in the two-dimensional hubbard model from weak to strong coupling, *Physical Review Research* **2**, 013108 (2020).
- [48] Y. Deng, E. Kozik, N. V. Prokof'ev, and B. V. Svistunov, Emergent BCS regime of the two-dimensional fermionic Hubbard model: Ground-state phase diagram, *Europhysics Letters* **110**, 57001 (2015).
- [49] I. Eremin, D. Manske, C. Joas, and K. H. Bennemann, Electronic theory for superconductivity in Sr_2RuO_4 : Triplet pairing due to spin-fluctuation exchange, *Europhysics Letters* **58**, 871 (2002).
- [50] E. Pavarini, I. Dasgupta, T. Saha-Dasgupta, O. Jepsen, and O. K. Andersen, Band-structure trend in hole-doped cuprates and correlation with $t_{c,\text{max}}$, *Physical Review Letters* **87**, 047003 (2001).
- [51] D. J. Scalapino, A common thread: The pairing interaction for unconventional superconductors, *Reviews of Modern Physics* **84**, 1383 (2012).
- [52] A. V. Chubukov, D. Pines, and J. Schmalian, A spin fluctuation model for d -wave superconductivity, in *The Physics of Superconductors*, edited by K.-H. Bennemann and J. B. Ketterson (Springer, 2003) pp. 495–590.
- [53] T. Moriya and K. Ueda, Spin fluctuations and high temperature superconductivity, *Advances in Physics* **49**, 555

- (2000).
- [54] P. Monthoux and D. Pines, Spin-fluctuation-induced superconductivity and normal-state properties of $\text{YBa}_2\text{Cu}_3\text{O}_7$, *Phys. Rev. B* **49**, 4261 (1994).
- [55] J. Brinckmann and P. A. Lee, Slave boson approach to neutron scattering in $\text{YBa}_2\text{Cu}_3\text{O}_{6+y}$ superconductors, *Phys. Rev. Lett.* **82**, 2915 (1999).
- [56] M. Wallerberger, S. Badr, S. Hoshino, S. Huber, F. Kakizawa, T. Koretsune, Y. Nagai, K. Nogaki, T. Nomoto, H. Mori, J. Otsuki, S. Ozaki, T. Plaikner, R. Sakurai, C. Vogel, N. Witt, K. Yoshimi, and H. Shinaoka, sparse-ir: Optimal compression and sparse sampling of many-body propagators, *SoftwareX* **21**, 101266 (2023).
- [57] M. Klett, J. Beyer, D. Riegler, J. Seufert, P. Wölfle, S. Rachel, and R. Thomale, Incommensurate magnetic order: A fingerprint for electronic correlations in hole-doped cuprates, *Phys. Rev. B* **110**, 085104 (2024).
- [58] M. Kitatani, N. Tsuji, and H. Aoki, Flex+dmft approach to the d -wave superconducting phase diagram of the two-dimensional hubbard model, *Phys. Rev. B* **92**, 085104 (2015).
- [59] S. Benhabib, A. Sacuto, M. Civelli, I. Paul, M. Cazayous, Y. Gallais, M.-A. Méasson, R. D. Zhong, J. Schneeloch, G. D. Gu, D. Colson, and A. Forget, Collapse of the normal-state pseudogap at a lifshitz transition in the $\text{bi}_2\text{sr}_2\text{cacu}_2\text{o}_{8+\delta}$ cuprate superconductor, *Phys. Rev. Lett.* **114**, 147001 (2015).
- [60] A. Piriou, N. Jenkins, C. Berthod, I. Maggio-Aprile, and Ø. Fischer, First direct observation of the van hove singularity in the tunnelling spectra of cuprates, *Nat. Commun.* **2**, 221 (2011).
- [61] M. Horio, K. Hauser, Y. Sassa, et al., Three-dimensional fermi surface of overdoped la-based cuprates, *Phys. Rev. Lett.* **121**, 077004 (2018).
- [62] J. G. Storey, J. L. Tallon, and G. V. M. Williams, Saddle-point van hove singularity and the phase diagram of high- T_c cuprates, *Phys. Rev. B* **76**, 174522 (2007).
- [63] J. P. Carbotte, Properties of boson-exchange superconductors, *Rev. Mod. Phys.* **62**, 1027 (1990).
- [64] Y. Wang, A. Abanov, B. L. Altshuler, E. A. Yuzbashyan, and A. V. Chubukov, Superconductivity near a quantum-critical point: The special role of the first matsubara frequency, *Physical Review Letters* **117**, 157001 (2016).
- [65] Y.-M. Wu, A. Abanov, Y. Wang, and A. V. Chubukov, Special role of the first matsubara frequency for superconductivity near a quantum critical point: Nonlinear gap equation below T_c and spectral properties in real frequencies, *Physical Review B* **99**, 144512 (2019).
- [66] D. Manske, I. Eremin, and K. H. Bennemann, Renormalization of the elementary excitations in hole- and electron-doped cuprates due to spin fluctuations, *Phys. Rev. B* **67**, 134520 (2003).
- [67] A. Abanov, A. V. Chubukov, and J. Schmalian, Quantum-critical theory of the spin-fermion model and its application to cuprates: Normal state analysis, *Advances in Physics* **52**, 119 (2003), <https://doi.org/10.1080/0001873021000057123>.
- [68] H. J. Vidberg and J. W. Serene, Solving the eliashberg equations by means of n -point padé approximants, *Journal of Low Temperature Physics* **29**, 179 (1977).
- [69] J. Baker, George A., *Essentials of Padé Approximants* (Academic Press, New York, 1975).
- [70] T. Dahm and L. Tewordt, Quasiparticle and spin excitation spectra in the normal and d -wave superconducting state of the two-dimensional hubbard model, *Physical Review Letters* **74**, 793 (1995).
- [71] Y. Gao, Robust a_1 superconductivity in the kagome lattice, *Physical Review B* **109**, 214501 (2024).
- [72] T. Valla, T. E. Kidd, J. D. Rameau, H.-J. Noh, G. D. Gu, P. D. Johnson, H.-B. Yang, and H. Ding, Fine details of the nodal electronic excitations in $\text{bi}_2\text{sr}_2\text{cacu}_2\text{o}_{8+\delta}$, *Phys. Rev. B* **73**, 184518 (2006).
- [73] T. Valla, I. K. Drozdov, and G. D. Gu, Disappearance of superconductivity due to vanishing coupling in overdoped $\text{bi}_2\text{sr}_2\text{cacu}_2\text{o}_{8+\delta}$, *Nat. Commun.* **11**, 569 (2020).
- [74] H. F. Fong, P. Bourges, Y. Sidis, L. P. Regnault, J. Bossy, A. Ivanov, D. L. Milius, I. A. Aksay, and B. Keimer, Spin susceptibility in underdoped $\text{YBa}_2\text{Cu}_3\text{O}_{6+x}$, *Phys. Rev. B* **61**, 14773 (2000).
- [75] S. Brehm, E. Arrigoni, M. Aichhorn, and W. Hanke, Theory of two-particle excitations and the magnetic susceptibility in high- t_c cuprate superconductors, *Europhysics Letters* **89**, 27005 (2010).

Supplemental Material for Slave-boson Formalism for Superconducting Pairing at Strong Coupling

Sarbajit Mazumdar,¹ Jonas Issing,¹ Jannis Seufert,¹ David Riegler,^{2,1} Peter Wölfle,² Ronny Thomale,¹ and Michael Klett^{1,*}

¹*Institut für Theoretische Physik und Astrophysik and Würzburg-Dresden Cluster of Excellence ctd.qmat, Julius-Maximilians-Universität Würzburg, Am Hubland, Campus Süd, Würzburg 97074, Germany*

²*Institut für Theorie der Kondensierten Materie, Karlsruhe Institute of Technology, D-76128 Karlsruhe, Germany*

(Dated: May 27, 2026)

SUPPLEMENTARY CONTENTS

Supplementary Contents	S1
S1. Slave-boson observables	S1
A. SRIKR representation	S2
B. Hamiltonian and effective action	S2
C. Physical charge and spin observables	S3
S2. Antisymmetrized pairing vertex and singlet/triplet projection	S4
A. Cooper-pair vertex and fermionic antisymmetry	S4
B. Density and spin decomposition	S4
C. Singlet/triplet projection	S5
D. Second-order fluctuation-mediated approximation	S6
S3. Mean-field equations	S6
A. BCS mean-field decoupling	S6
B. Static finite-temperature gap equation	S6
C. Parity constraints and free energy	S7
S4. Expansion in the basis and numerical solution	S7
A. Form-factor basis	S7
B. Projection of the dynamic gap equation	S8
C. Iterative fixed-point solver	S8
D. Identification of the leading symmetry channel	S9
E. Working equations	S10
F. Benchmark results	S11
S5. Frequency-dependent gap profile	S11
A. Padé analytic continuation	S11

S1. SLAVE-BOSON OBSERVABLES

For completeness, we summarize the spin-rotation-invariant Kotliar–Ruckenstein (SRIKR) slave-boson formulation used in the main text. We focus on the definitions needed to identify the charge and spin observables entering the Gaussian fluctuation analysis.

* michael.klett@uni-wuerzburg.de

A. SRIKR representation

At each lattice site i , the enlarged local Hilbert space is generated by pseudofermions $f_{i\sigma}$ and slave bosons $e_i, d_i, p_{i\mu}$, with $\mu = 0, 1, 2, 3$. The bosons e_i and d_i describe the empty and doubly occupied states, while the spin-rotation-invariant singly occupied sector is encoded in the 2×2 matrix

$$p_i^\dagger = \frac{1}{2} \sum_{\mu=0}^3 p_{i\mu}^\dagger \tau^\mu = \frac{1}{2} \begin{pmatrix} p_{i0}^\dagger + p_{i3}^\dagger & p_{i1}^\dagger - ip_{i2}^\dagger \\ p_{i1}^\dagger + ip_{i2}^\dagger & p_{i0}^\dagger - p_{i3}^\dagger \end{pmatrix}, \quad (\text{S1.1})$$

where τ^0 is the 2×2 identity matrix and $\tau^{1,2,3}$ are Pauli matrices. The physical local states are represented as

$$|0\rangle_i = e_i^\dagger |\text{vac}\rangle, \quad |\sigma\rangle_i = \sum_{\sigma'} p_{i,\sigma\sigma'}^\dagger f_{i\sigma'}^\dagger |\text{vac}\rangle, \quad |2\rangle_i = d_i^\dagger f_{i\uparrow}^\dagger f_{i\downarrow}^\dagger |\text{vac}\rangle. \quad (\text{S1.2})$$

The physical Hilbert space is selected by the local constraints

$$1 = e_i^\dagger e_i + d_i^\dagger d_i + \sum_{\mu=0}^3 p_{i\mu}^\dagger p_{i\mu}, \quad (\text{S1.3a})$$

$$\sum_{\sigma} f_{i\sigma}^\dagger f_{i\sigma} = \sum_{\mu=0}^3 p_{i\mu}^\dagger p_{i\mu} + 2d_i^\dagger d_i, \quad (\text{S1.3b})$$

$$\sum_{\sigma\sigma'} \tau_{\sigma\sigma'} f_{i\sigma'}^\dagger f_{i\sigma} = p_{i0}^\dagger \mathbf{p}_i + \mathbf{p}_i^\dagger p_{i0} - i \mathbf{p}_i^\dagger \times \mathbf{p}_i. \quad (\text{S1.3c})$$

Here $\mathbf{p}_i = (p_{i1}, p_{i2}, p_{i3})^\top$. The physical electron operator is expressed in terms of pseudofermions as

$$c_{i\sigma}^\dagger = \sum_{\sigma'} z_{i,\sigma\sigma'}^\dagger f_{i\sigma'}^\dagger, \quad c_{i\sigma} = \sum_{\sigma'} f_{i\sigma'} z_{i,\sigma'\sigma}. \quad (\text{S1.4})$$

Following the original Kotliar–Ruckenstein operator ordering, the spin-rotation-invariant renormalization matrix is taken as

$$z_i = \sqrt{2} L_i \left(e_i^\dagger p_i + \tilde{p}_i^\dagger d_i \right) R_i, \quad (\text{S1.5})$$

with

$$z_i^\dagger = \sqrt{2} R_i \left(p_i^\dagger e_i + d_i^\dagger \tilde{p}_i \right) L_i. \quad (\text{S1.6})$$

The matrices p_i and \tilde{p}_i are defined by

$$p_i = \frac{1}{2} \left(p_{i0} \tau^0 + \sum_{a=1}^3 p_{ia} \tau^a \right), \quad \tilde{p}_i = \frac{1}{2} \left(p_{i0} \tau^0 - \sum_{a=1}^3 p_{ia} \tau^a \right). \quad (\text{S1.7})$$

The left and right normalization matrices are

$$L_i = \left[\left(1 - d_i^\dagger d_i \right) \tau^0 - 2p_i^\dagger p_i \right]^{-1/2}, \quad R_i = \left[\left(1 - e_i^\dagger e_i \right) \tau^0 - 2\tilde{p}_i^\dagger \tilde{p}_i \right]^{-1/2}. \quad (\text{S1.8})$$

All products in Eqs. (S1.5)–(S1.8) are matrix products in spin space, and the inverse square roots are understood as matrix inverse square roots. The normalization factors L_i and R_i ensure the correct noninteracting limit and reproduce the Gutzwiller quasiparticle renormalization at the saddle point.

B. Hamiltonian and effective action

We start from the one-band Hubbard model

$$H = \sum_{ij,\sigma} c_{i\sigma}^\dagger t_{ij} c_{j\sigma} - \mu \sum_i \hat{n}_i + U \sum_i c_{i\uparrow}^\dagger c_{i\downarrow}^\dagger c_{i\downarrow} c_{i\uparrow}. \quad (\text{S1.9})$$

After the SRIKR substitution, the interacting term becomes $U d_i^\dagger d_i$, while the kinetic term is renormalized by the z -matrices. In momentum space, the resulting fermionic Hamiltonian can be written as

$$H_{\text{SB}} = \sum_{\mathbf{k}_1, \mathbf{k}_2} \mathbf{f}_{\mathbf{k}_1}^\dagger H_{\mathbf{k}_1, \mathbf{k}_2}[\psi] \mathbf{f}_{\mathbf{k}_2} + U \sum_i d_i^\dagger d_i, \quad (\text{S1.10})$$

with $\mathbf{f}_{\mathbf{k}} = (f_{\mathbf{k}\uparrow}, f_{\mathbf{k}\downarrow})^\text{T}$ and

$$H_{\mathbf{k}_1, \mathbf{k}_2}[\psi] = -\mu \delta_{\mathbf{k}_1, \mathbf{k}_2} \mathbb{1}_2 + \frac{1}{N} \sum_{\mathbf{k}} (z^\dagger)_{\mathbf{k}-\mathbf{k}_1}^\text{T} \mathcal{H}_{\mathbf{k}}(z)_{\mathbf{k}-\mathbf{k}_2}^\text{T}. \quad (\text{S1.11})$$

The collective bosonic field is denoted by

$$\psi = (e, d, p_0, \mathbf{p}, \alpha, \beta_0, \boldsymbol{\beta}), \quad (\text{S1.12})$$

where α , β_0 , and $\boldsymbol{\beta}$ are Lagrange multipliers enforcing the constraints in Eq. (S1.3). The partition function is written as a coherent-state path integral,

$$Z = \int \mathcal{D}[f^*, f] \mathcal{D}[\psi^*, \psi] e^{-\mathcal{S}[f, \psi]}, \quad \mathcal{S} = \int_0^{1/T} d\tau (\mathcal{L}_{\text{B}} + \mathcal{L}_{\text{F}}). \quad (\text{S1.13})$$

The bosonic and fermionic parts of the Euclidean Lagrangian are

$$\begin{aligned} \mathcal{L}_{\text{B}} = \sum_i & \left[d_i^* (\partial_\tau + U) d_i + e_i^* \partial_\tau e_i + p_{0,i}^* \partial_\tau p_{0,i} + \mathbf{p}_i^* \cdot \partial_\tau \mathbf{p}_i \right. \\ & + i\alpha_i (e_i^* e_i + p_{0,i}^* p_{0,i} + \mathbf{p}_i^* \cdot \mathbf{p}_i + d_i^* d_i - 1) \\ & - i\beta_{0,i} (p_{0,i}^* p_{0,i} + \mathbf{p}_i^* \cdot \mathbf{p}_i + 2d_i^* d_i) \\ & \left. - i\boldsymbol{\beta}_i \cdot (p_{0,i}^* \mathbf{p}_i + \mathbf{p}_i^* p_{0,i} - i \mathbf{p}_i^* \times \mathbf{p}_i) \right], \end{aligned} \quad (\text{S1.14a})$$

$$\mathcal{L}_{\text{F}} = \sum_{\mathbf{k}_1, \mathbf{k}_2} \mathbf{f}_{\mathbf{k}_1}^\dagger [\partial_\tau \delta_{\mathbf{k}_1, \mathbf{k}_2} + H_{\mathbf{k}_1, \mathbf{k}_2}[\psi]] \mathbf{f}_{\mathbf{k}_2}. \quad (\text{S1.14b})$$

Integrating out the pseudofermions gives the bosonic effective action

$$\mathcal{S}_{\text{eff}}[\psi] = \int_0^{1/T} d\tau \mathcal{L}_{\text{B}} - \text{Tr} \ln [\partial_\tau + H[\psi]], \quad (\text{S1.15})$$

which is the starting point for the saddle-point and Gaussian fluctuation analysis. After a local $SU(2) \times U(1) \times U(1)$ gauge transformation, we work in the radial gauge. In this gauge, the phases of e , p_0 , and \mathbf{p} are gauged away, so that these fields can be chosen real, while the doublon field d remains complex. The corresponding gauge fields appear as the Lagrange multipliers α , β_0 , and $\boldsymbol{\beta}$, which enforce the local SRIKR constraints. The fermionic kernel then acquires the local constraint fields explicitly,

$$H_{\mathbf{k}_1, \mathbf{k}_2}[\psi] = -\mu \mathbb{1}_2 \delta_{\mathbf{k}_1, \mathbf{k}_2} + \frac{1}{\sqrt{N}} (\beta_0 \tau^0 + \boldsymbol{\beta} \cdot \boldsymbol{\tau})_{\mathbf{k}_1 - \mathbf{k}_2}^\text{T} + \frac{1}{N} \sum_{\mathbf{k}} (z^\dagger)_{\mathbf{k}-\mathbf{k}_1}^\text{T} \mathcal{H}_{\mathbf{k}}(z)_{\mathbf{k}-\mathbf{k}_2}^\text{T}. \quad (\text{S1.16})$$

C. Physical charge and spin observables

The physical spin density is

$$\hat{\mathbf{S}}_i = \frac{1}{2} \sum_{\sigma\sigma'} c_{i\sigma}^\dagger \boldsymbol{\tau}_{\sigma\sigma'} c_{i\sigma'}. \quad (\text{S1.17})$$

Using the SRIKR constraints, it can be represented purely in terms of the spin slave bosons as

$$\hat{\mathbf{S}}_i = \frac{1}{2} \left(p_{0,i}^\dagger \check{\mathbf{p}}_i + \check{\mathbf{p}}_i^\dagger p_{0,i} - i \check{\mathbf{p}}_i^\dagger \times \check{\mathbf{p}}_i \right), \quad \check{\mathbf{p}}_i = (p_{1,i}, -p_{2,i}, p_{3,i})^\text{T}. \quad (\text{S1.18})$$

In the radial gauge this reduces to the simple form

$$\hat{\mathbf{S}}_i \rightarrow p_{0,i} \check{\mathbf{P}}_i. \quad (\text{S1.19})$$

The physical density operator is

$$\hat{n}_i = \sum_{\sigma} c_{i\sigma}^{\dagger} c_{i\sigma} = \sum_{\sigma} f_{i\sigma}^{\dagger} f_{i\sigma} = 1 + d_i^{\dagger} d_i - e_i^{\dagger} e_i. \quad (\text{S1.20})$$

Thus, charge fluctuations are encoded in the scalar slave-boson sector, whereas spin fluctuations are encoded in the vector p_a sector. Expanding Eq. (S1.15) around the saddle point, $\psi = \bar{\psi} + \delta\psi$, gives the Gaussian fluctuation action

$$\delta\mathcal{S}^{(2)} = \sum_q \delta\psi_{\mu}(-q) \mathcal{M}_{\mu\nu}(q) \delta\psi_{\nu}(q), \quad (\text{S1.21})$$

where $\mathcal{M}(q)$ is the inverse propagator of the slave-boson fluctuations. The physical response functions are obtained by projecting the inverse fluctuation matrix onto the corresponding charge or spin vertices:

$$\chi_{s/c}(q) = \sum_{\mu,\nu} \mathcal{C}_{s/c}^{\mu\nu} \mathcal{M}_{\mu\nu}^{-1}(q). \quad (\text{S1.22})$$

The coefficients $\mathcal{C}_{s/c}^{\mu\nu}$ are fixed by Eqs. (S1.18) and (S1.20). In the paramagnetic saddle point, the spin and charge sectors decouple. Consequently, the transverse spin response is obtained from the (p_a, β_a) block of \mathcal{M}^{-1} , while the charge response follows from the block spanned by the scalar bosons and their associated Lagrange multipliers. Further details of this construction can be found in Refs. [43, 44].

S2. ANTISYMMETRIZED PAIRING VERTEX AND SINGLET/TRIPLET PROJECTION

This section provides the derivation of the singlet and triplet pairing vertices used in the main text, Eqs. (10) and (9), starting from a general antisymmetrized two-particle vertex.

A. Cooper-pair vertex and fermionic antisymmetry

We consider the effective scattering of a Cooper pair $(\mathbf{k}, \alpha; -\mathbf{k}, \beta) \rightarrow (\mathbf{k}', \gamma; -\mathbf{k}', \delta)$ and define the corresponding pairing vertex $\mathcal{V}_{\alpha\beta\gamma\delta}^{\text{pair}}(k, k')$, where $k = (i\omega_n, \mathbf{k})$ and $k' = (i\omega_{n'}, \mathbf{k}')$. Two bosonic momentum-frequency transfers appear naturally,

$$q \equiv k - k', \quad q' \equiv k + k'.$$

Fermionic antisymmetry requires

$$\mathcal{V}_{\alpha\beta\gamma\delta}^{\text{pair}}(k, k') = -\mathcal{V}_{\alpha\beta\delta\gamma}^{\text{pair}}(k, -k'). \quad (\text{S2.1})$$

Since the effective interactions constructed from charge and spin susceptibilities depend only on the transferred four-momentum, exchanging the outgoing fermions maps $q \leftrightarrow q'$.

B. Density and spin decomposition

Assuming SU(2) spin-rotation invariance, the most general direct particle-particle interaction can be written as

$$\Gamma_{\alpha\beta\gamma\delta}(q) = \mathcal{V}^{nn}(q) \delta_{\alpha\gamma} \delta_{\beta\delta} + \mathcal{V}^{ss}(q) \boldsymbol{\tau}_{\alpha\gamma} \cdot \boldsymbol{\tau}_{\beta\delta}.$$

Antisymmetrizing with respect to the outgoing legs yields

$$\begin{aligned} \mathcal{V}_{\alpha\beta\gamma\delta}^{\text{pair}}(k, k') &= \Gamma_{\alpha\beta\gamma\delta}(q) - \Gamma_{\alpha\beta\delta\gamma}(q') \\ &= \left[\mathcal{V}^{nn}(q) \delta_{\alpha\gamma} \delta_{\beta\delta} - \mathcal{V}^{nn}(q') \delta_{\alpha\delta} \delta_{\beta\gamma} \right] \\ &\quad + \left[\mathcal{V}^{ss}(q) \boldsymbol{\tau}_{\alpha\gamma} \cdot \boldsymbol{\tau}_{\beta\delta} - \mathcal{V}^{ss}(q') \boldsymbol{\tau}_{\alpha\delta} \cdot \boldsymbol{\tau}_{\beta\gamma} \right]. \end{aligned} \quad (\text{S2.2})$$

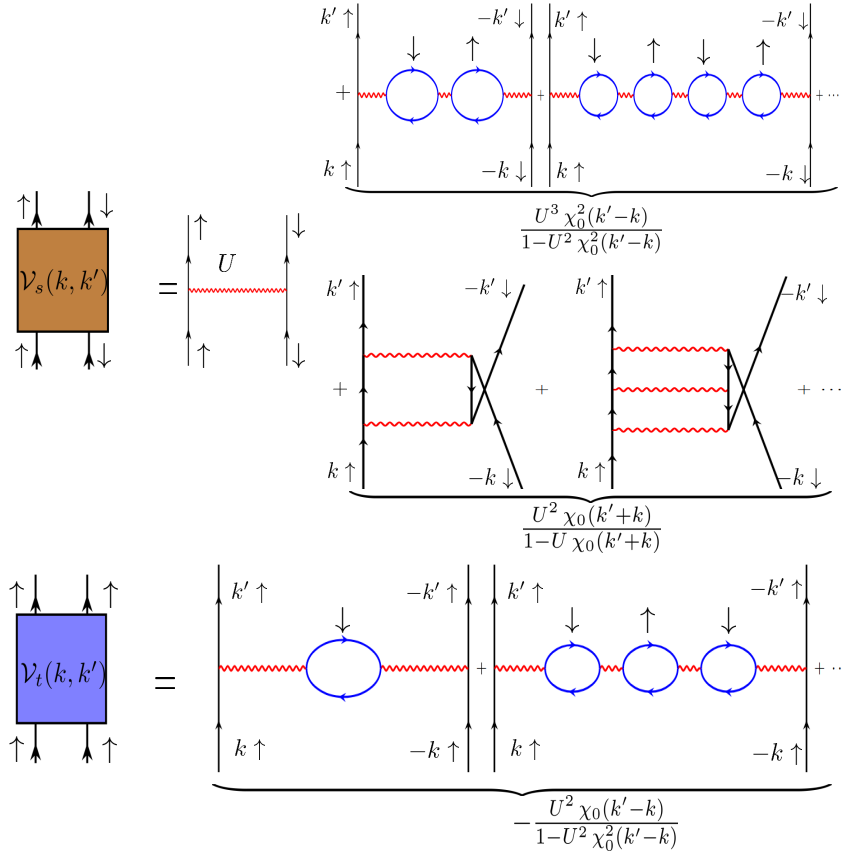


FIG. S2.1. **Structure of the fluctuation-mediated pairing vertex.** Schematic diagram of the direct ($q = k - k'$) and exchange ($q' = k + k'$) contributions entering the antisymmetrized Cooper-pair interaction. The decomposition into density and spin channels, followed by projection onto singlet and triplet sectors, leads to the effective vertices in Eqs. (S2.6) and (S2.7).

C. Singlet/triplet projection

Define the standard singlet and triplet pairing matrices

$$\Phi_{\alpha\beta}^{(s)} \equiv (i\tau^y)_{\alpha\beta}, \quad \Phi_{\alpha\beta}^{(t),i} \equiv (i\tau^y \tau^i)_{\alpha\beta}, \quad i = x, y, z.$$

The SU(2)-invariant decomposition of the Cooper vertex then reads

$$\mathcal{V}_{\alpha\beta\gamma\delta}^{\text{pair}}(k, k') = \mathcal{V}_s(k, k') \Phi_{\alpha\beta}^{(s)} \Phi_{\gamma\delta}^{(s)\dagger} + \mathcal{V}_t(k, k') \sum_{i=x,y,z} \Phi_{\alpha\beta}^{(t),i} \Phi_{\gamma\delta}^{(t),i\dagger}. \quad (\text{S2.3})$$

Projecting Eq. (S2.2) onto equal-spin and opposite-spin channels gives

$$\mathcal{V}_t(k, k') = \frac{1}{2} [\mathcal{V}^{nn}(q) - \mathcal{V}^{nn}(q')] + \frac{1}{2} [\mathcal{V}^{ss}(q) - \mathcal{V}^{ss}(q')], \quad (\text{S2.4})$$

and

$$\mathcal{V}_s(k, k') = \frac{1}{2} [\mathcal{V}^{nn}(q) + \mathcal{V}^{nn}(q')] - \frac{3}{2} [\mathcal{V}^{ss}(q) + \mathcal{V}^{ss}(q')]. \quad (\text{S2.5})$$

The exchange terms proportional to q' implement the antisymmetry constraint of Eq. (S2.1).

D. Second-order fluctuation-mediated approximation

Within the spin-fluctuation framework used in the main text, we approximate the effective interaction to second order in an effective onsite scale U_{eff} . Writing again $q = k - k'$ and $q' = k + k'$, the triplet vertex becomes

$$\mathcal{V}_t(k, k') = \frac{1}{4} U_{\text{eff}}^2 \left[\chi_s(q') + \chi_c(q') - \chi_s(q) - \chi_c(q) \right], \quad (\text{S2.6})$$

while the singlet vertex is

$$\mathcal{V}_s(k, k') = U_{\text{eff}} - \frac{1}{4} U_{\text{eff}}^2 \left[\chi_c(q) + \chi_c(q') \right] + \frac{3}{4} U_{\text{eff}}^2 \left[\chi_s(q) + \chi_s(q') \right]. \quad (\text{S2.7})$$

For a local Hubbard interaction the bare $\mathcal{O}(U_{\text{eff}}^-)$ term contributes only to the singlet channel, while the q' terms implement the antisymmetrization required by Eq. (S2.1). Our choice of vertex structure is motivated by the effective RPA summation of bubble and ladder diagrams shown schematically in Fig. S2.1; expanding the corresponding RPA-dressed interactions to $\mathcal{O}(U_{\text{eff}}^2)$ yields Eqs. (S2.6) and (S2.7).

S3. MEAN-FIELD EQUATIONS

This section summarizes the static mean-field gap equation that follows from the pairing interaction discussed above and that is referred to in the main text when discussing the static approximation to the full dynamic gap equation.

A. BCS mean-field decoupling

We start from a generic momentum-space pairing Hamiltonian,

$$H = \sum_{\mathbf{k}, \sigma} \xi(\mathbf{k}) c_{\mathbf{k}\sigma}^\dagger c_{\mathbf{k}\sigma} + \frac{1}{2} \sum_{\mathbf{k}\mathbf{k}'} \sum_{\alpha\beta\gamma\delta} \mathcal{V}_{\alpha\beta\gamma\delta}(\mathbf{k}, \mathbf{k}') c_{\mathbf{k}\alpha}^\dagger c_{-\mathbf{k}\beta}^\dagger c_{-\mathbf{k}'\delta} c_{\mathbf{k}'\gamma}, \quad (\text{S3.1})$$

where $\xi(\mathbf{k}) = \varepsilon(\mathbf{k}) - \mu$. The superconducting order parameter is defined as

$$\Delta_{\alpha\beta}(\mathbf{k}) \equiv - \sum_{\mathbf{k}'\gamma\delta} \mathcal{V}_{\alpha\beta\gamma\delta}(\mathbf{k}, \mathbf{k}') \langle c_{-\mathbf{k}'\delta} c_{\mathbf{k}'\gamma} \rangle. \quad (\text{S3.2})$$

Performing the standard BCS decoupling gives the mean-field Hamiltonian

$$\begin{aligned} H_{\text{MF}} = & \sum_{\mathbf{k}, \sigma} \xi(\mathbf{k}) c_{\mathbf{k}\sigma}^\dagger c_{\mathbf{k}\sigma} - \frac{1}{2} \sum_{\mathbf{k}} \sum_{\alpha\beta} \left[c_{\mathbf{k}\alpha}^\dagger c_{-\mathbf{k}\beta}^\dagger \Delta_{\alpha\beta}(\mathbf{k}) + \Delta_{\alpha\beta}^*(\mathbf{k}) c_{-\mathbf{k}\beta} c_{\mathbf{k}\alpha} \right] \\ & - \frac{1}{2} \sum_{\mathbf{k}\mathbf{k}'} \sum_{\alpha\beta\gamma\delta} \Delta_{\alpha\beta}^*(\mathbf{k}) [\mathcal{V}^{-1}]_{\alpha\beta\gamma\delta}(\mathbf{k}, \mathbf{k}') \Delta_{\gamma\delta}(\mathbf{k}'). \end{aligned} \quad (\text{S3.3})$$

For pure singlet or triplet states the quasiparticle energy reduces to

$$E_{s/t}(\mathbf{k}) = \sqrt{\xi(\mathbf{k})^2 + |\Delta_{s/t}(\mathbf{k})|^2}.$$

B. Static finite-temperature gap equation

Using Eq. (S3.2) together with the anomalous thermal expectation value, the finite-temperature self-consistency condition can be written as

$$\Delta_{\alpha\beta}(\mathbf{k}) = - \sum_{\mathbf{k}'\gamma\delta} \mathcal{V}_{\alpha\beta\gamma\delta}(\mathbf{k}, \mathbf{k}') \frac{\Delta_{\gamma\delta}(\mathbf{k}')}{2E(\mathbf{k}')} \tanh\left(\frac{E(\mathbf{k}')}{2T}\right). \quad (\text{S3.4})$$

Projecting the gap into singlet and triplet sectors,

$$\Delta_{\alpha\beta}(\mathbf{k}) = \Delta_s(\mathbf{k}) (i\tau^y)_{\alpha\beta} + \Delta_t^i(\mathbf{k}) (i\tau^y\tau^i)_{\alpha\beta}, \quad (\text{S3.5})$$

one obtains the decoupled static gap equations

$$\Delta_{s/t}(\mathbf{k}) = - \sum_{\mathbf{k}'} \mathcal{V}_{s/t}(\mathbf{k}, \mathbf{k}') \frac{\Delta_{s/t}(\mathbf{k}')}{2E_{s/t}(\mathbf{k}')} \tanh\left(\frac{E_{s/t}(\mathbf{k}')}{2T}\right), \quad (\text{S3.6})$$

with

$$E_{s/t}(\mathbf{k}) = \sqrt{\xi(\mathbf{k})^2 + |\Delta_{s/t}(\mathbf{k})|^2}. \quad (\text{S3.7})$$

Equation (S3.6) is the static limit of the full dynamic gap equation, Eq. (12) in the main text, obtained by neglecting the bosonic-frequency dependence of the interaction and the fermionic-frequency dependence of the gap.

C. Parity constraints and free energy

The Pauli principle requires

$$\Delta_{\alpha\beta}(\mathbf{k}) = -\Delta_{\beta\alpha}(-\mathbf{k}). \quad (\text{S3.8})$$

Therefore a pure singlet state satisfies

$$\Delta_s(\mathbf{k}) = \Delta_s(-\mathbf{k}),$$

while a pure triplet state satisfies

$$\Delta_t^i(\mathbf{k}) = -\Delta_t^i(-\mathbf{k}).$$

The corresponding mean-field free energy functional is

$$\mathcal{F} = \sum_{\mathbf{q}} \left\{ -2T \ln[1 + e^{-\beta E_{s/t}(\mathbf{q})}] + \frac{1}{2} \frac{|\Delta_{s/t}(\mathbf{q})|^2}{E_{s/t}(\mathbf{q})} \tanh\left(\frac{E_{s/t}(\mathbf{q})}{2T}\right) - E_{s/t}(\mathbf{q}) + \xi(\mathbf{q}) \right\} + \mu N, \quad (\text{S3.9})$$

and minimizing \mathcal{F} with respect to $\Delta_{s/t}(\mathbf{k})$ reproduces Eq. (S3.6).

S4. EXPANSION IN THE BASIS AND NUMERICAL SOLUTION

To solve the full dynamic gap equation, Eq. (12) in the main text, we expand the gap function in a set of lattice harmonics and determine the corresponding Matsubara-frequency-dependent coefficients self-consistently.

A. Form-factor basis

We expand the gap function in a finite set of lattice harmonics,

$$\Delta(\mathbf{k}, i\omega_n) = \sum_{\alpha=1}^M c_{\alpha}(i\omega_n) \varphi_{\alpha}(\mathbf{k}), \quad (\text{S4.1})$$

where $c_{\alpha}(i\omega_n)$ are frequency-dependent expansion coefficients and $\varphi_{\alpha}(\mathbf{k})$ denotes the corresponding momentum-space form factor. The form-factor basis used in this work is summarized in Table S4.1.

TABLE S4.1. Form-factor basis used in the expansion of $\Delta(\mathbf{k}, i\omega_n)$. The irreducible representations are given for the square-lattice point group with inversion parity.

Channel α	Form factor $\varphi_\alpha(\mathbf{k})$	Parity	Irrep
s	1	even	A_{1g}
$s^{(1)}$	$\cos k_x + \cos k_y$	even	A_{1g}
$s^{(2)}$	$\cos 2k_x + \cos 2k_y$	even	A_{1g}
$d_{x^2-y^2}$	$\cos k_x - \cos k_y$	even	B_{1g}
d_{xy}	$\sin k_x \sin k_y$	even	B_{2g}
$d_{xy}^{(2)}$	$\sin k_x \sin 2k_y + \sin 2k_x \sin k_y$	even	B_{2g}
$d_{x^2-y^2}^{(2)}$	$\cos 2k_x - \cos 2k_y$	even	B_{1g}
$d_{x^2-y^2}^{(3)}$	$\cos 2k_x \cos k_y - \cos 2k_y \cos k_x$	even	B_{1g}
g	$(\cos k_x - \cos k_y) \sin k_x \sin k_y$	even	A_{2g}
p_x	$\sin k_x$	odd	E_u
p_y	$\sin k_y$	odd	E_u
p'_x	$(\cos k_x - \cos k_y) \sin k_x$	odd	E_u
p'_y	$-(\cos k_x - \cos k_y) \sin k_y$	odd	E_u
\vdots	\vdots	\vdots	\vdots

The basis contains onsite and extended s -wave harmonics, several d -wave harmonics, a g -wave harmonic, and odd-parity p -wave form factors. The extended p' -wave sector is included as the doublet (p'_x, p'_y) , so that the basis remains closed under the square-lattice point-group operations.

B. Projection of the dynamic gap equation

Projecting Eq. (12) onto the basis functions gives

$$c_\beta(i\omega_n) = -\frac{T}{\mathcal{N}_\beta} \sum_{m,\alpha} \Gamma_{\beta\alpha}(n, m; \{c\}) c_\alpha(i\omega_m), \quad (\text{S4.2})$$

where

$$\mathcal{N}_\beta = \int_{\text{BZ}} \frac{d^2k}{(2\pi)^2} |\varphi_\beta(\mathbf{k})|^2$$

and

$$\Gamma_{\beta\alpha}(n, m; \{c\}) = \int_{\text{BZ}} \frac{d^2k d^2p}{(2\pi)^4} \varphi_\beta^*(\mathbf{k}) \mathcal{V}(\mathbf{k} - \mathbf{p}, i\omega_n - i\omega_m) \varphi_\alpha(\mathbf{p}) \frac{1}{\omega_m^2 + \xi_{\mathbf{p}}^2 + \left| \sum_\gamma c_\gamma(i\omega_m) \varphi_\gamma(\mathbf{p}) \right|^2}. \quad (\text{S4.3})$$

Equations (S4.2) and (S4.3) define the nonlinear fixed-point problem for the coefficient vector $\mathbf{c}(i\omega_n)$.

C. Iterative fixed-point solver

We solve Eq. (S4.2) iteratively using linear mixing. Starting from an initial seed $\mathbf{c}^{(0)}(i\omega_n)$, the updated coefficients are obtained from the fixed-point map defined by Eq. (S4.2), followed by a mixing step

$$c_\beta^{(t)}(i\omega_n) = (1 - \eta) c_\beta^{(t-1)}(i\omega_n) + \eta \tilde{c}_\beta^{(t)}(i\omega_n),$$

with mixing parameter $\eta \in (0, 1]$. The iteration is stopped once the Euclidean norm of the difference between successive iterates falls below a prescribed tolerance.

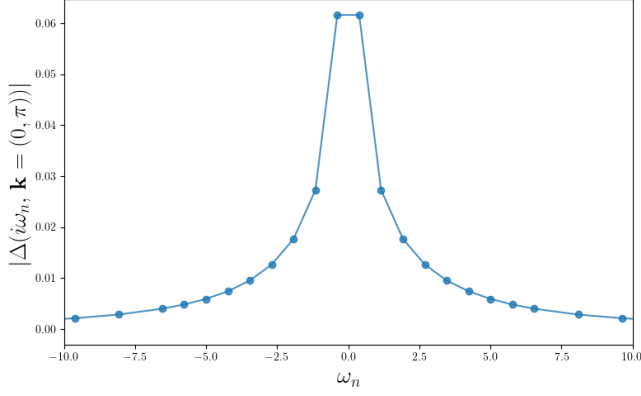


FIG. S4.1. Representative converged Matsubara-frequency dependence of the leading superconducting gap amplitude at $\mathbf{k} = (0, \pi)$.

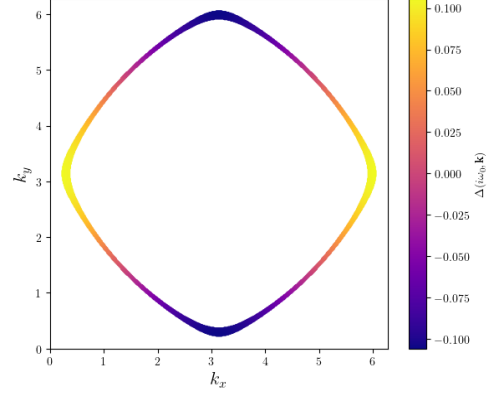


FIG. S4.2. Projection of $d_{x^2-y^2}$ gap structure onto the Fermi surface.

1. Initialize the coefficient vector $\mathbf{c}^{(0)}(i\omega_n)$.
2. For $t = 1, 2, \dots, \mathbb{T}_{\max}$, construct

$$\Delta^{(t-1)}(\mathbf{p}, i\omega_m) = \sum_{\gamma} c_{\gamma}^{(t-1)}(i\omega_m) \varphi_{\gamma}(\mathbf{p}).$$

3. Using $\Delta^{(t-1)}(\mathbf{p}, i\omega_m)$, assemble the kernel

$$\Gamma_{\beta\alpha}(n, m; \{\mathbf{c}^{(t-1)}\})$$

from Eq. (S4.3).

4. Compute the updated coefficients $\tilde{c}_{\beta}^{(t)}(i\omega_n)$ from Eq. (S4.2).
5. Apply linear mixing according to

$$c_{\beta}^{(t)} = (1 - \eta)c_{\beta}^{(t-1)} + \eta\tilde{c}_{\beta}^{(t)}.$$

6. Check for convergence. If

$$\|\mathbf{c}^{(t)} - \mathbf{c}^{(t-1)}\|_2 < \text{tol},$$

then stop and take $\mathbf{c}^{(t)}$ as the self-consistent solution.

7. If convergence is not reached, continue the iteration until $t = \mathbb{T}_{\max}$.
8. If the procedure does not converge within \mathbb{T}_{\max} steps, take

$$\mathbf{c}^{(\mathbb{T}_{\max})}$$

as the final approximate solution.

D. Identification of the leading symmetry channel

Once a converged solution is obtained, we identify the leading pairing symmetry from the largest overlap with the basis functions at the lowest Matsubara frequency,

$$\alpha_{\text{lead}} = \arg \max_{\alpha} |\text{overlap}_{\alpha}(i\omega_0)|, \quad |\text{overlap}_{\text{lead}}| = \max_{\alpha} |\text{overlap}_{\alpha}(i\omega_0)|. \quad (\text{S4.4})$$

Figures S4.1 and S4.2 show a representative converged solution and the associated Fermi-surface gap structure.

To benchmark the qualitative frequency and symmetry structure obtained from the slave-boson-based pairing kernel, we also implemented a standard single-band FLEX+RPA calculation.

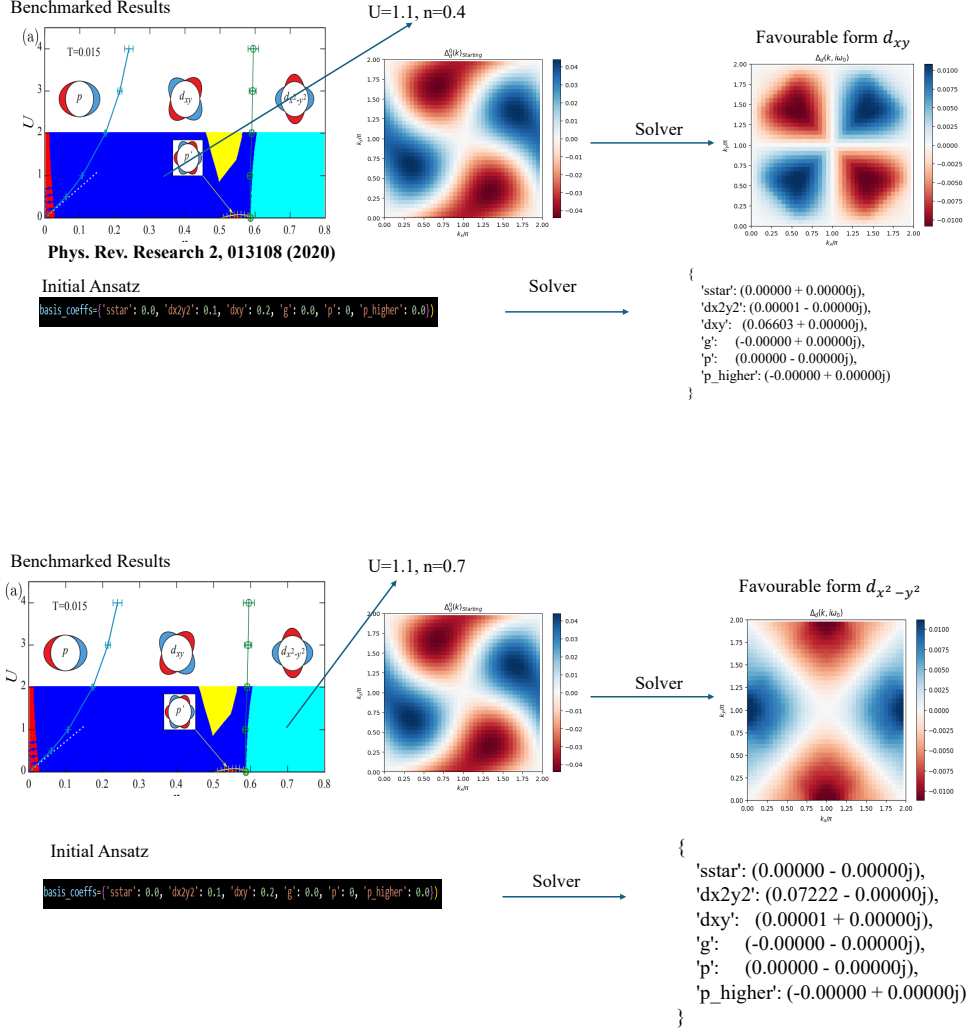


FIG. S4.3. **Benchmark of the solver against the FLEX+RPA phase diagram.** The phase diagram shown in the left panels is taken from Ref. [47]. For the filling $n = 0.4$ & $n = 0.7$ and interaction strength $U = 1.1$, two different initial ansätze were supplied to the solver in order to test whether the expected pairing symmetry is recovered. **Top row:** starting from an initial ansatz with dominant d_{xy} component, the solver converges to a gap function with the characteristic d_{xy} sign structure, consistent with the favourable pairing channel in that region of the phase diagram. **Bottom row:** starting from an initial ansatz with dominant $d_{x^2-y^2}$ component, the solver correspondingly converges to a gap function with $d_{x^2-y^2}$ symmetry. The rightmost panels show the converged momentum dependence of the gap function $\Delta(\mathbf{k})$, while the printed coefficient sets display the numerical weights of the symmetry components after convergence. This comparison serves as a benchmark that the solver correctly identifies and stabilizes the intended pairing representation when initialized in the corresponding channel.

E. Working equations

We use the square-lattice dispersion

$$\varepsilon_{\mathbf{k}} = -2t(\cos k_x + \cos k_y) - 4t' \cos k_x \cos k_y, \quad (\text{S4.5})$$

and define $\xi_{\mathbf{k}} = \varepsilon_{\mathbf{k}} - \mu$. With $k = (\mathbf{k}, i\omega_n)$ and $q = (\mathbf{q}, i\nu_m)$, the dressed Green's function is

$$G(k) = \frac{1}{i\omega_n - \xi_{\mathbf{k}} - \Sigma(k)}. \quad (\text{S4.6})$$

The irreducible bubble is

$$\chi^0(q) = -\frac{T}{N} \sum_k G(k+q) G(k), \quad (\text{S4.7})$$

and the RPA-resummed spin and charge susceptibilities are

$$\chi^s(q) = \frac{\chi^0(q)}{1 - U\chi^0(q)}, \quad \chi^c(q) = \frac{\chi^0(q)}{1 + U\chi^0(q)}. \quad (\text{S4.8})$$

The FLEX effective interaction and the self-energy update are

$$\mathcal{V}_{\text{eff}}(q) = \frac{3}{2}U^2\chi^s(q) + \frac{1}{2}U^2\chi^c(q) - U^2\chi^0(q) + U, \quad (\text{S4.9})$$

$$\Sigma(k) = \frac{T}{N} \sum_q \mathcal{V}_{\text{eff}}(q) G(k-q). \quad (\text{S4.10})$$

The singlet pairing interaction used in the linearized gap equation is

$$\mathcal{V}^{(s)}(q) = \frac{3}{2}U^2\chi^s(q) - \frac{1}{2}U^2\chi^c(q) + U, \quad (\text{S4.11})$$

and the leading eigenvalue λ and eigenfunction $\Delta(k)$ satisfy

$$\lambda \Delta(k) = -\frac{T}{N} \sum_{k'} \mathcal{V}^{(s)}(k-k') G(k') G(-k') \Delta(k'). \quad (\text{S4.12})$$

The superconducting transition temperature is estimated from $\lambda(T_c) = 1$.

F. Benchmark results

Representative leading eigenfunctions from the FLEX+RPA calculation are shown in Figs. S4.3. In both cases, the extracted gap structure agrees with the target square-lattice symmetry and serves as a benchmark for the symmetry assignment used in the main text.

S5. FREQUENCY-DEPENDENT GAP PROFILE

This section summarizes the Padé analytic continuation used in the main text to extract real-frequency information from the Matsubara-axis gap solutions.

A. Padé analytic continuation

Starting from the Matsubara data $\{z_n = i\omega_n, \Delta(i\omega_n)\}$ at fixed momentum \mathbf{k}_0 , we approximate the gap by a Padé rational function

$$P_N(z) = \frac{A_N(z)}{B_N(z)}, \quad (\text{S5.1})$$

constructed to interpolate the computed Matsubara points. The real-frequency gap is then obtained as

$$\Delta(\omega) = \lim_{\eta \rightarrow 0^+} P_N(\omega + i\eta), \quad (\text{S5.2})$$

with a small finite η retained in practice for numerical stability. Following Refs. [68, 69], the Padé approximant is represented in continued-fraction form. Defining coefficients $\{a_n\}$ and recursion polynomials $A_n(z)$, $B_n(z)$, the stable continued-fraction construction reads

$$A_{n+1}(z) = A_n(z) + (z - z_n)a_{n+1}A_{n-1}(z), \quad B_{n+1}(z) = B_n(z) + (z - z_n)a_{n+1}B_{n-1}(z).$$

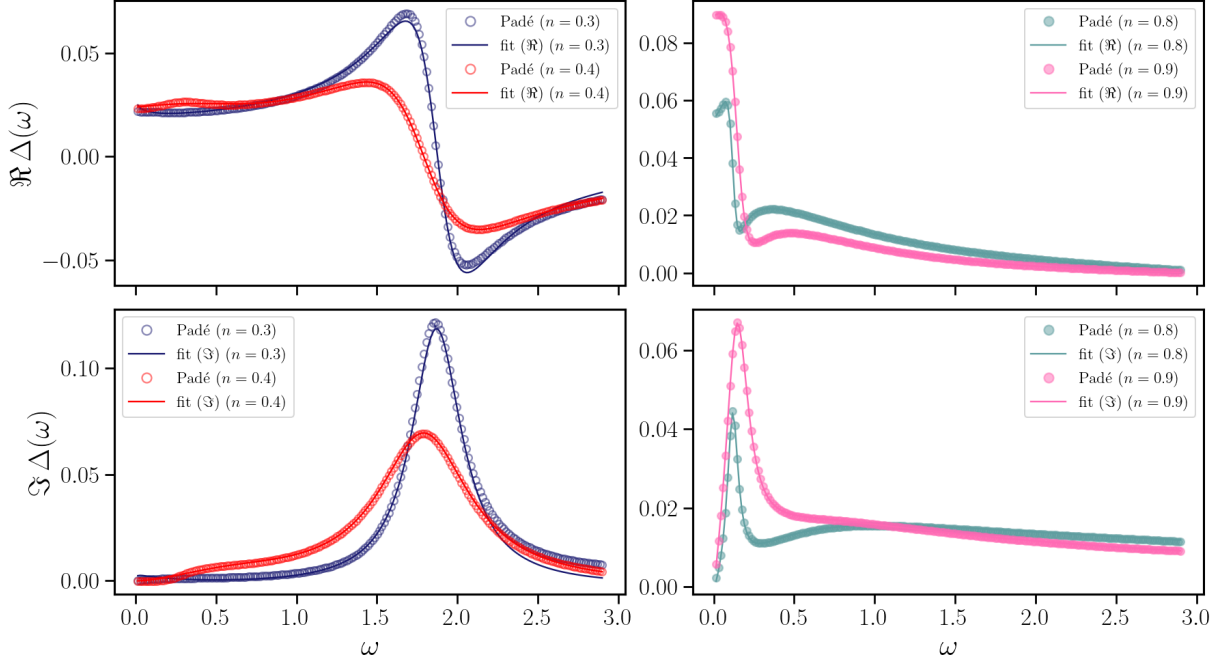


FIG. S4.4. **Representative Padé analytic continuation of the dynamic gap.** Illustration of the continuation procedure for $U = 2$ and $t' = -0.2$. The figure shows the gap data after the Padé reconstruction, and the resulting real- and imaginary-part structure on the real-frequency axis used in the analysis of the peak scale discussed in the main text.

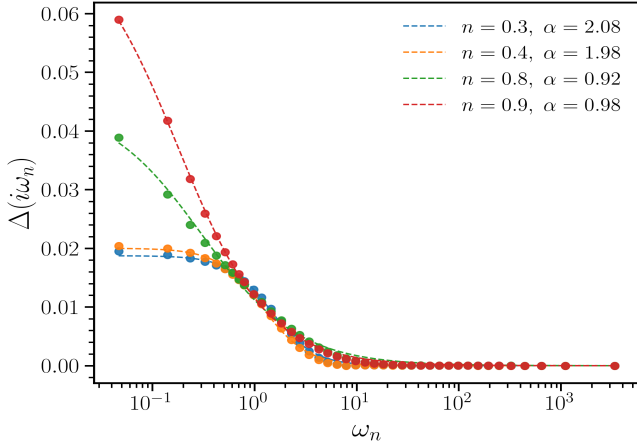


FIG. S4.5. **Matsubara-frequency dependence of the leading superconducting gap.** Matsubara-frequency dependence of the leading superconducting gap for $U = 2$ and $t' = -0.2$ at different fillings ($T \rightarrow 0$). Closer to the $d_{x^2-y^2}$ regime, $\alpha \sim 1$ is consistent with pairing dominated by strong antiferromagnetic fluctuations, while larger α values in the low-density d_{xy} sector indicate a more rapidly decaying effective interaction in frequency space.

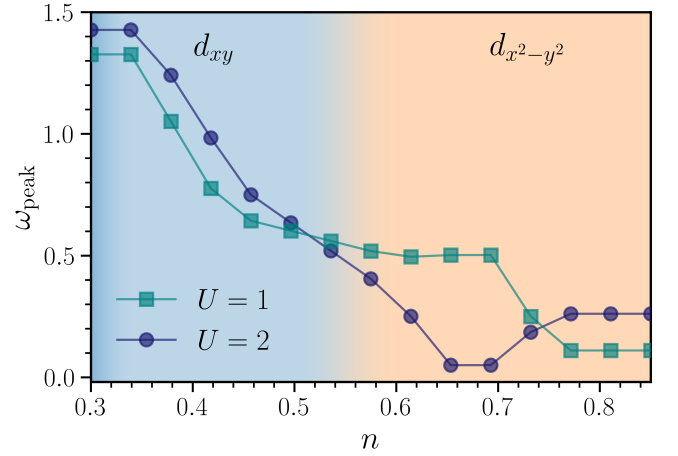


FIG. S4.6. **FLEX+RPA result for the real-frequency gap peak scale.** Similar analysis as in the slave-boson calculation, but performed for FLEX+RPA data at the same band parameters ($t' = -0.2$) and interactions ($U = 1, 2$). The peak position ω_{peak} of $\Re \Delta(\omega)$ shows the same overall softening trend with filling and a corresponding change across the $d_{xy} \rightarrow d_{x^2-y^2}$ transition.

For numerical stability one propagates the ratios

$$\bar{A}_n(z) = \frac{A_n(z)}{A_{n-1}(z)}, \quad \bar{B}_n(z) = \frac{B_n(z)}{B_{n-1}(z)},$$

so that the Padé approximant can be built recursively while controlling round-off errors at large order. To assess the stability of the analytically continued real-frequency gap, we repeated the Padé continuation for several Padé orders

N , broadening parameters η , and real-frequency fitting windows. The qualitative filling dependence of ω_{peak} remains unchanged under moderate variations of these numerical parameters. In particular, the downward shift of ω_{peak} with increasing filling and the change in slope near the $d_{xy} \rightarrow d_{x^2-y^2}$ crossover are robust for both SB & FLEX+RPA (Fig. S4.6).
